Thermodynamic Investigation into the Mechanisms of Proton-Coupled Electron Transfer Events in Heme Protein Maquettes†

Amit R. Reddi, Charles J. Reedy, Steven Mui, and Brian R. Gibney*

Department of Chemistry, Columbia University, 3000 Broadway, MC 3121, New York, New York 10027

Received August 8, 2006; Revised Manuscript Received November 1, 2006

ABSTRACT: To study the engineering requirements for proton pumping in energy-converting enzymes such as cytochrome *c* oxidase, the thermodynamics and mechanisms of proton-coupled electron transfer in two designed heme proteins are elucidated. Both heme protein maquettes chosen, heme *b*−$[H10A24]_2$ and heme *b*−$[\Delta 7\text{-His}]_2$, are four-α-helix bundles that display pH-dependent heme midpoint potential modulations, or redox-Bohr effects. Detailed equilibrium binding studies of ferric and ferrous heme *b* with these maquettes allow the individual contributions of heme−protein association, iron−histidine ligation, and heme−protein electrostatics to be elucidated. These data demonstrate that the larger, less well-structured $[H10A24]_2$ binds heme *b* in both oxidation states tighter than the smaller and more well-structured $[\Delta 7\text{-His}]_2$ due to a stronger porphyrin−protein hydrophobic interaction. The 66 mV (1.5 kcal/mol) difference in their heme reduction potentials observed at pH 8.0 is due mostly to stabilization of ferrous heme in $[H10A24]_2$ relative to $[\Delta 7\text{-His}]_2$. The data indicate that porphyrin−protein hydrophobic interactions and heme iron coordination are responsible for the K_d value of 37 nM for the heme *b*−$[\Delta 7\text{-His}]_2$ scaffold, while the affinity of heme *b* for $[H10A24]_2$ is 20-fold tighter due to a combination of porphyrin−protein hydrophobic interactions, iron coordination, and electrostatic effects. The data also illustrate that the contribution of bis-His coordination to ferrous heme protein affinity is limited, <3.0 kcal/mol. The $1H^+/1e^-$ redox-Bohr effect of heme *b*−$[H10A24]_2$ is due to the greater absolute stabilization of the ferric heme (4.1 kcal/mol) compared to the ferrous heme (1.4 kcal/mol) binding upon glutamic acid deprotonation, i.e., an electrostatic response mechanism. The $2H^+/1e^-$ redox-Bohr effect observed for heme *b*−$[\Delta 7\text{-His}]_2$ is due to histidine protonation and histidine dissociation of ferrous heme *b* upon reduction, i.e., a ligand loss mechanism. These results indicate that the contribution of porphyrin−protein hydrophobic interactions to heme affinity is critical to maintaining the heme bound in both oxidation states and eliciting an electrostatic response from these designed heme protein scaffolds.

Proton-coupled electron transfer is a fundamental component of the proton pumps involved in biochemical energy transduction (*1*−*3*). Redox-linked acid−base equilibria, or redox-Bohr effects, are responsible for the proton pumping action of respiratory complexes I, III, and IV: NADH-ubiquinone oxidoreductase, ubiquinol-cytochrome *c* oxidoreductase, and cytochrome *c* oxidase, respectively (*4*−*6*). While placing acid or base groups into low dielectrics shifts their pK_a values, further shifts are induced upon cofactor oxidation or reduction due to the electrostatic response to the formal change in charge (*7*). In the case of the Mitchell Q-cycle quinones, large pK_a shifts are observed because the cofactor binds protons directly as it is reduced from the quinone to the semiquinone and quinol states whose respective pK_a values are −7, +5, and +12 (*8, 9*). In the case of metal cofactors which bind protons on their ligands or on local amino acids, proton binding to and release from local bases and acids partially compensate for the change in local charge upon oxidation and reduction (*10*, *11*). In these cases, the electrostatic response that attempts to maintain electroneutrality results in the observation of more modest pK_a shifts (*12*, *13*).

Studies on iron−sulfur and heme proteins reveal a diversity of mechanisms and stoichiometries of proton−electron coupling. In natural iron−sulfur proteins, the $1H^+/1e^-$ event at the $[3Fe\text{-}4S]^{+/0}$ center in *Azotobacter vinelandii* ferredoxin I (AvFdI) is due to a local aspartic acid, while the $2H^+/1e^-$ event at the complex III-type $[2Fe\text{-}2S]^{2+/+}$ Reiske protein from *Thermus thermophilus* is due to the histidine N^ϵ atoms that are not directly coordinated to the iron (*14*−*16*). In natural heme proteins, monoheme cytochrome *c*″ displays a $1H^+/1e^-$ coupled event due to histidine ligand protonation and dissociation, while the multi-heme cytochrome c_3 species display $2H^+/2e^-$ coupled events localized to a heme propionate and a noncoordinating histidine (*17*−*19*). In de novo designed proteins, proton-coupled electron transfer reactivity at both iron−sulfur and heme active sites has also been observed (*20*−*23*). The best described redox-Bohr effect is in heme *b*−$[H10A24]_2$, a designed heme protein that shows two distinct $1H^+/1e^-$ proton-coupled electron transfer events due to glutamic acid and lysine protonation. While the effect of proton binding near each of these metal sites in modulating the reduction potential is described well, the redox-Bohr sites

† This work was supported by an American Heart Association grant to B.R.G. (0455900T). A.R.R. acknowledges receipt of a National Science Foundation GK-12 Fellowship (DGE-02-31875).

* To whom correspondence should be addressed. E-mail: brg@chem.columbia.edu. Phone: (212) 854-6346. Fax: (212) 932-1289.

10.1021/bi061607g CCC: $37.00
Published on Web 12/13/2006

and proton/electron stoichiometries are variable depending on the protein scaffold. Furthermore, the underlying effects of proton binding on the absolute stability of the two metal cofactor oxidation states are not well understood.

Our approach to clarifying the structure−function relationships in the natural respiratory complexes, such as proton coupling to heme reduction in cytochrome *c* oxidase (*24*−*26*), is to evaluate the equilibrium thermodynamics of metal−cofactor affinity and electrochemistry in simplified de novo designed proteins, or maquettes (*27*). By measuring the absolute thermodynamic affinity of designed protein scaffolds for ferric and ferrous hemes along with their related electrochemistry, we are elucidating the fundamental factors that govern the reduction potentials of hemes in biology (*28*). We have designed a stably folded four-α-helix bundle, $[\Delta 7\text{-His}]_2$ or $[\Delta 7\text{-H}_{10}\text{I}_{14}\text{I}_{21}]_2$, and measured the absolute affinity of its two bis-His heme binding sites for ferric and ferrous heme *b* (*29*). As observed for many designed heme proteins (*30*), heme *b*−$[\Delta 7\text{-His}]_2$ displays spectroscopic properties similar to those of natural bis-His coordinated *b*-type cytochromes, e.g., the cytochrome *b* subunit of the cytochrome bc_1 complex (*31*). Using this approach, we have demonstrated that axial ligand basicity affects ferric and not ferrous heme affinities and that electron-withdrawing substituents on porphyrins elevate reduction potentials by destabilizing the ferric heme with little alteration in ferrous heme affinity (*32*−*34*).

Herein, we report the effect of the protein scaffold and its response to solution pH on the ferric and ferrous heme *b* affinities and the bound heme electrochemistry of two designed heme proteins, $[\Delta 7\text{-His}]_2$ and $[\text{H10A24}]_2$, in examining the fundamental basis for their redox-Bohr effects. The reduction potentials measured at various pH values demonstrate that the scaffolds exhibit distinct redox-Bohr events. Detailed equilibrium thermodynamic measurements of the ferric and ferrous heme *b* affinities of the two scaffolds reveal the individual contributions of porphyrin−protein hydrophobic interactions, heme iron coordination, and protein electrostatics to the observed conditional dissociation constant values and midpoint reduction potentials. The heme dissociation constant, K_d, values over a wide pH range also reveal the mechanistic basis for the observed proton-coupled electron transfer events in each scaffold and provide a rationale for their differences. These data provide a global description of the effect of protons and electrons on the absolute affinity of each heme protein maquette scaffold for ferric and ferrous heme *b* and the resulting redox-Bohr events.

MATERIALS AND METHODS

Reagents. Fmoc-protected amino acids were obtained from Bachem. HBTU, *O*-(1*H*-benzotriazol-1-yl)-*N*,*N*,*N*′,*N*′-tetramethyluronium hexafluorophosphate, was purchased from Qbiogene. Guanidine hydrochloride (8 M) was used as received from Pierce. All other chemicals and solvents were reagent grade.

General Procedure for the Preparation of Peptides. The peptide ligands were synthesized by solid phase peptide synthesis and purified to homogeneity as previously described (*33*−*35*). The primary structures of the helices in each peptide are, as follows: H10A24, Ac-CGGGELWKLHEELLKKFEELLKLAEERLKKL-$CONH_2$; Δ7-His, Ac-CGGGEIWKLHEEFIKLFEERIKKL-$CONH_2$.

UV−*Vis Spectroscopy.* UV−visible spectra were recorded on Varian Cary 100 or Perkin-Elmer Lambda 25 spectrophotometers using quartz cells with path lengths of 1.0 and 10 cm. Peptide concentrations were determined spectrophotometrically using an ϵ_{280} of 5600 M^{-1} cm^{-1} per helix.

Heme Redox Potentiometry. Chemical redox titrations were performed as previously described with all values reported relative to the standard hydrogen electrode (*36*). Titrations were performed in aqueous solutions containing 4 μM heme protein in 20 mM buffer and 100 mM KCl over the pH range of 4.0−8.0. The following buffers were used: KP_i (pH > 6.6), MES (5.5 < pH < 6.5), and citrate (pH < 5.0).

pH Dependence of the Peptide-Bound Heme b Reduction Potential As Determined by Heme Redox Potentiometry. The reduction potential as a function of pH for $[\text{H10A24}]_2$ shows two distinct proton-coupled electron transfer events with 60 mV per pH slopes indicative of a $1H^+/1e^-$ coupled event (*20*). The data between pH 8.0 and 3.0 are best fit to an equilibrium model in which there is a one-proton/one-electron electrochemical event.

$$E_{meas} = E_{acid} - \frac{RT}{nF}\ln\frac{1 + 10^{-pH+pK_a^{red}}}{1 + 10^{-pH+pK_a^{ox}}} \quad (1)$$

where E_{meas} is the measured reduction potential at a given pH, E_{acid} is the limiting reduction potential at low pH corresponding to the Fe(III)/Fe(II) couple of the fully protonated heme protein, and pK_a^{red} (7.0) and pK_a^{ox} (4.2) are the pK_a values in the reduced and oxidized states, respectively, of the residue that leads to the pH-dependent reduction potential. IR spectroscopy has been used to assign the residue responsible for the redox-Bohr effect to a glutamic acid (*20*).

The heme reduction potential as a function of pH for heme *b*−$[\Delta 7\text{-His}]_2$ displays a 120 mV per pH slope indicative of a $2H^+/1e^-$ coupled event. Thus, the data can be fit to a proton-coupled electron transfer model in which there is one two-proton/one-electron electrochemical event.

$$E_{meas} = E_{acid} - \frac{RT}{nF}\ln\frac{1 + 10^{-2pH+2pK_a^{red}}}{1 + 10^{-2pH+2pK_a^{ox}}} \quad (2)$$

Alternatively, the data may also be adequately described by a standard Henderson−Hasselbalch equation for the protonation of the two histidine residues and the concomitant dissociation of the heme group in the reduced state (*37*).

$$E_{meas} = E_{acid} - \Delta E\left(\frac{1}{10^{-pH+pK_a^{eff-red}} + 1} + \frac{1}{10^{-pH+pK_a^{eff-red}} + 1}\right) \quad (3)$$

where the midpoint reduction potential measured at any pH, E_{meas}, is a function of the midpoint potential at acidic pH values, E_{acid}, the change in midpoint reduction potential due to deprotonation, ΔE, the solution pH value, and the acid dissociation constant of the histidine ligands in the presence of metal, the effective pK_a value or $pK_a^{eff-red}$.

Potentiometric pH Titrations in Heme Affinity Studies. Potentiometric pH titrations were performed manually using

an anaerobic 1.0 cm path length cuvette fitted with a pH electrode under a stream of nitrogen gas. The pH of 3.0 μM heme protein samples in a combination buffer (20 mM HEPES, 20 mM MES, 20 mM citrate, and 100 mM KCl) was adjusted via addition of microliter aliquots of 6 N HCl. Between each addition, the samples were allowed to equilibrate for up to 20 min prior to measurement of the heme protein absorption by UV−vis spectroscopy. For the ferrous heme protein samples, sodium dithionite was added to ensure complete reduction prior to the start of the titration. The pH dependence of the Soret band absorbance at λ_{max} was fit to an equation for the cooperative protonation of the two heme ligating histidine residues, as shown for the oxidized state.

$$\mathrm{Abs_{meas}} = \mathrm{Abs_0} + \Delta\mathrm{Abs}\frac{1}{10^{-2\mathrm{pH}+2\mathrm{p}K_a^{\mathrm{eff-ox}}}+1} \quad (4)$$

where the absorbance measured at any pH, $\mathrm{Abs_{meas}}$, is a function of the initial absorbance, $\mathrm{Abs_0}$, the change in absorbance due to protonation, ΔAbs, the solution pH value, the number of protons involved in the process, two, and the acid dissociation constant of the ligands in the presence of metal, the effective pK_a value or p$K_a^{\mathrm{eff-ox}}$. An analogous equation for the reduced state provides the reduced state effective p$K_a^{\mathrm{eff-red}}$ value of the histidine ligands.

Ferric and Ferrous Heme b Conditional Dissociation Constants in Heme Affinity Studies. Ferric and ferrous heme *b* dissociation constants were determined over the pH range of 1.6−8.0 using previously reported titration methods (*29*). The buffers employed at various solution pHs were as follows: 20 mM KP_i and 100 mM KCl at pH 8.0, 20 mM HEPES and 100 mM KCl at pH >6.6, 20 mM MES and 100 mM KCl between pH 5.5 and 6.5, and 20 mM citrate and 100 mM KCl at pH <5.0. Equilibration times between additions varied from 20 min (pH >6.0) to overnight (pH <6.0). Ferrous heme samples were maintained at a reducing potential by addition of sodium dithionite prior to the start of the titration and by placing the anaerobic cuvette in a spectrophotometer within an Atmosbag (Sigma-Aldrich-Fluka, Milwaukee, WI) under a nitrogen atmosphere.

pH Dependence of the Conditional Dissociation Constants in Heme Affinity Studies. The conditional dissociation constants, K_d, measured as a function of pH for ferric and ferrous heme *b*−[H10A24]$_2$ were fit to an equilibrium binding expression based on the observed pH-dependent attenuation in heme affinity due to the protonation of three residues, one glutamate and two heme-bound histidines. The equation used to fit the ferric heme *b*−[H10A24]$_2$ dissociation constant data is as follows:

$$K_f^{\mathrm{cond-ox}} = K_f^{\mathrm{ox}}\frac{10^{-3\mathrm{pH}+\mathrm{p}K_a^{\mathrm{Glu}}+2\mathrm{p}K_a^{\mathrm{His}}} + 10^{-2\mathrm{pH}+\mathrm{p}K_a^{\mathrm{Glu}}+\mathrm{p}K_a^{\mathrm{His}}} + 10^{-\mathrm{pH}+\mathrm{p}K_a^{\mathrm{Glu}}}}{10^{-3\mathrm{pH}+\mathrm{p}K_a^{\mathrm{ox}}+2\mathrm{p}K_a^{\mathrm{eff-ox}}} + 10^{-2\mathrm{pH}+\mathrm{p}K_a^{\mathrm{ox}}+\mathrm{p}K_a^{\mathrm{eff-ox}}} + 10^{-\mathrm{pH}+\mathrm{p}K_a^{\mathrm{ox}}}} \quad (5)$$

where K_f^{ox} is the pH-independent formation constant at pH values where all three residues are deprotonated for ferric heme *b*−[H10A24]$_2$, $K_f^{\mathrm{cond-ox}}$ is the conditional formation constant at each solution pH which is equivalent to $1/K_d^{\mathrm{Fe(III)}}$, pK_a^{ox} is the glutamic acid pK_a value in ferric heme *b*−[H10A24]$_2$, pK_a^{Glu} is the glutamic acid pK_a value in apo-[H10A24]$_2$ (estimated to be greater than or equal to pK_a^{red}), pK_a^{His} is the pK_a values of the histidine residues in the apoprotein, and p$K_a^{\mathrm{eff-ox}}$ is the effective pK_a value of the histidine ligands in ferric heme *b*−[H10A24]$_2$ (determined from the potentiometric pH titration). An analogous equation was derived for the ferrous heme *b*−[H10A24]$_2$ protein with the corresponding pK_a^{red} and p$K_a^{\mathrm{eff-red}}$ values for the holoprotein and identical apoprotein values, pK_a^{Glu} and pK_a^{His}.

Scheme 1: Mechanisms of Shifting E_m^{bound} in the Positive Direction by Altering the Affinity of a Protein for the Oxidized Heme (gray) and Reduced Heme (black) States

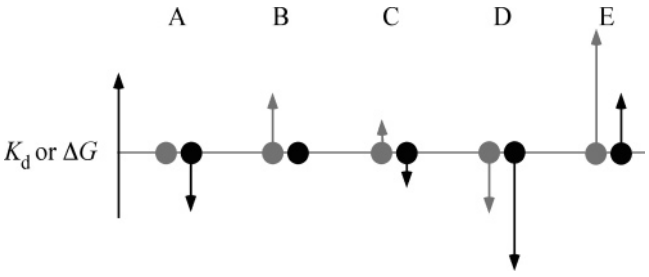

The pH dependence of the conditional dissociation constant, K_d, values of ferric and ferrous heme *b*−[Δ7-His]$_2$ were fit to an equilibrium binding expression based on the observed pH-dependent attenuation in heme binding due to the protonation of the two heme-ligating histidines. As such, the ferric heme *b*−[Δ7-His]$_2$ conditional dissociation constants, $K_d^{\mathrm{Fe(III)}}$, expressed as formation constants, $K_f^{\mathrm{cond-ox}}$, may be described in terms of solution pH, the pH-independent formation constant, K_f^{ox}, and the p$K_a^{\mathrm{eff-ox}}$ and pK_a^{His} values of the histidine residues in the oxidized heme protein and apoprotein states, respectively.

$$K_f^{\mathrm{cond-ox}} = K_f^{\mathrm{ox}}\frac{10^{-2\mathrm{pH}+2\mathrm{p}K_a^{\mathrm{His}}} + 10^{-\mathrm{pH}+\mathrm{p}K_a^{\mathrm{His}}}}{10^{-2\mathrm{pH}+2\mathrm{p}K_a^{\mathrm{eff-ox}}} + 10^{-\mathrm{pH}+\mathrm{p}K_a^{\mathrm{eff-ox}}}} \quad (6)$$

An analogous equation was used for the ferrous heme *b*−[Δ7-His]$_2$ protein data with a corresponding p$K_a^{\mathrm{eff-red}}$ value and an identical apoprotein pK_a^{His} value.

RESULTS

Experimental Design. The midpoint reduction potential of heme bound to a protein, E_m^{bound}, is fundamentally governed by the ratio of the ferric and ferrous heme dissociation constant values, $K_d^{\mathrm{Fe(III)}}$ and $K_d^{\mathrm{Fe(II)}}$, respectively, and the reduction potential of the unbound heme, E_m^{free}, as follows (*39*):

$$E_m^{\mathrm{bound}} = E_m^{\mathrm{free}} + \frac{RT}{nF}\ln\left[\frac{K_d^{\mathrm{Fe(III)}}}{K_d^{\mathrm{Fe(II)}}}\right] \quad (7)$$

As with all redox cofactor-containing proteins, the reduction potential of the heme reflects the relative affinities of the protein for the heme in the two oxidation states (*40*−*42*). In addition, the heme reduction potential also reflects the difference in the global stabilities of the holoprotein fold in the two oxidation states (*43*−*45*). Structural modifications that cause changes in E_m^{bound} result from a stabilization or destabilization of either one or both of the heme iron oxidation states. As illustrated in Scheme 1, any one of five

mechanisms can account for a positive shift in the value of E_m^{bound} between heme proteins: (A) stabilization of the reduced state (black), (B) destabilization of the oxidized state (gray), (C) stabilization of the reduced state with destabilization of the oxidized state, (D) stabilization of both states but greater stabilization of the reduced state, and (E) destabilization of both states with greater destabilization of the oxidized state. While the relative stabilization of the reduced state over the oxidized state is constant in mechanisms A−E of Scheme 1, the magnitudes of the absolute (de)stabilizations are highly variable.

Using the truncated heme protein maquette scaffold, $[\Delta 7\text{-His}]_2$, we have determined the mechanisms by which various structural factors alter ferric and ferrous heme affinities and thereby modulate their midpoint reduction values (*46*, *47*). These efforts rely on our ability to accurately measure the absolute affinities of $[\Delta 7\text{-His}]_2$ for both ferric and ferrous heme *b* (*29*). This ability is relatively rare among heme proteins whose thermodynamic affinities are usually only measured in the ferric oxidation state and which may be undeterminable due to kinetic trapping of the heme (*48*−*51*). By measuring the heme electrochemistry and the absolute affinities of oxidized and reduced hemes in $[\Delta 7\text{-His}]_2$ and its variants, we have elucidated the mechanisms used by the axial ligands and the heme type to modulate the bound heme reduction potentials. For instance, changing the axial ligands from histidine to β-(4-pyridyl)-L-alanine in a heme *b* maquette increases the E_m value by 287 mV via mechanism C, while using Fe(diacetyldeuteroporphyrin IX) rather than heme *b* in a bis-histidine maquette scaffold results in a +160 mV shift due to mechanism B (*33*, *47*). Thus, individual structural modifications to a heme protein may alter the E_m value by different mechanisms from Scheme 1.

The design of the $[\Delta 7\text{-His}]_2$ sequence is based on the prototype two-heme protein maquette, $[H10A24]_2$, whose architecture is a noncovalent dimer of disulfide-bridged di-α-helical peptides or $(\alpha\text{-SS-}\alpha)_2$ (*27*). Since the minimalist design of the $[H10A24]_2$ helices is based on four repeats of seven amino acids, or heptads (*abcdefg*), truncation was accomplished by deleting the central heptad which does not include the heme-binding histidine residues (*52*). Additionally, several leucine residues were replaced with β-branched isoleucine residues to improve the conformational specificity of the apoprotein scaffold as evaluated by NMR spectroscopy (*29*). The resulting peptide, $[\Delta 7\text{-His}]_2$, is smaller than the Dutton maquettes, comparable in size to the combinatorial library of heme proteins developed by Hecht and co-workers, and larger than peptidyl−porphyrin complexes (*53*−*55*). The $[\Delta 7\text{-His}]_2$ scaffold is less stable and more well-structured than the molten globule-like $[H10A24]_2$ in the apo state, and both scaffolds are stable to pH over the range of 1.0−11.0 as evaluated by CD spectroscopy (*27*).

For this study, we have selected these two different bis-His heme *b* protein maquettes, heme *b*−$[\Delta 7\text{-His}]_2$ and the related heme *b*−$[H10A24]_2$ prototype, to evaluate the role of the pH response of the protein scaffold in modulating heme affinities and reduction potentials. While both of these scaffolds contain two heme binding sites, we chose to limit our study to the maquettes with only a single heme bound to simplify the analysis. This was achieved by addition of only 0.9 equiv of heme to the four-helix bundle. These heme proteins were selected for the difference in their single heme

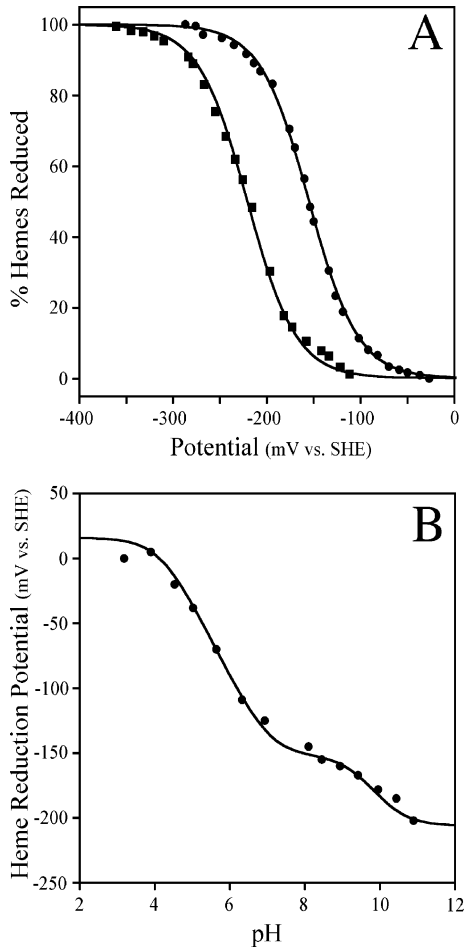

FIGURE 1: Comparison of the redox activity of the heme *b*−$[H10A24]_2$ (●) and heme *b*−$[\Delta 7\text{-His}]_2$ (■) heme−protein maquettes. (A) Redox potentiometry data for both at pH 8.0 are fit to single $N = 1$ Nernst curves with midpoint reduction potentials of -156 ± 10 and -222 ± 10 mV, respectively. Both experiments were performed in 20 mM KP_i, 100 mM KCl, pH 8.0 buffer at 25 °C. (B) Effect of solution pH on the reduction potential of heme *b*−$[H10A24]_2$ (●). A glutamic acid, pK_a^{ox} value of 4.2 and pK_a^{red} value of 7.0, shifts the heme midpoint potential by −150 mV between pH 4.0 and 8.0. A lysine residue, pK_a^{ox} and pK_a^{red} values of 9.4 and 10.3, respectively, shifts the reduction potential by −47 mV between pH 9.0 and 11.

reduction potentials at pH 8.0 as well as for the observation of proton-coupled electron transfer in the latter (*20*). Figure 1A shows that heme *b*−$[\Delta 7\text{-His}]_2$ and heme *b*−$[H10A24]_2$ have E_m values at pH 8.0 of −222 and −156 mV, respectively. The reduction potential value of heme *b*−$[\Delta 7\text{-His}]_2$ (−222 mV) is close to the value of the bis-imidazole complex of heme *b* in aqueous solution which suggests that both hemes are solvent accessible. The observed 66 mV shift in E_m between the two maquettes represents a 1.5 kcal/mol change in the ratio of the ferric and ferrous K_d values due to the thermodynamic relationship $\Delta\Delta G = -nF \times \Delta E_m$.

In terms of proton-coupled electron transfer, the reduction potentials of $[H10A24]_2$ containing one heme *b* or two hemes *b* are pH-dependent with the Pourbaix diagram for the former presented in Figure 1B (*20*). Two distinct $1H^+/1e^-$ proton coupling events are observed: one assigned by IR spectroscopy to a glutamic acid residue with oxidized and reduced state pK_a values of 4.2 and 7.0, respectively, and a second one ascribed to a lysine residue with oxidized and reduced state pK_a values of 9.4 and 10.3, respectively. Since the

majority of the E_m modulation in heme $b-[H10A24]_2$ is due to the glutamic acid residue, our efforts focused below pH 8.0. In addition, we chose to study the scaffolds with only a single heme bound to avoid the complications due to the observed heme−heme electrostatic effects and the presence of multiple K_d values for each oxidation state, i.e., $K_{d1}^{Fe(III)}$ and $K_{d2}^{Fe(III)}$.

In this study, we evaluate the role of the protein scaffold and its response to solution pH in altering the ferric and ferrous heme affinity of these two maquettes to probe their mechanisms of proton-coupled electron transfer. The effect of solution pH on the reduction potential of heme $b-[\Delta7\text{-His}]_2$ was determined for comparison to the heme $b-[H10A24]_2$ redox-Bohr effect. These data were coupled with the absolute affinities of the two heme protein maquette scaffolds for both ferric and ferrous heme *b* in an effort to describe the effect of scaffold protonation on their absolute ferric and ferrous heme *b* affinities. While both scaffolds exhibit proton-coupled electron transfer events, detailed thermodynamic data reveal that their mechanisms for proton coupling are distinct. This is due in large part to the differences in the energetics of porphyrin−protein hydrophobic interactions between the two scaffolds. The data also reveal that the 66 mV shift in E_m between the two maquettes results from the stabilization of both ferrous heme $b-[H10A24]_2$ and ferric heme $b-[H10A24]_2$ relative to heme $b-[\Delta7\text{-His}]_2$, or mechanism D of Scheme 1.

Redox Activity Comparison of Heme b Bound to the [Δ7-His]₂ and [H10A24]₂ Maquette Scaffolds. The pH dependence of the heme $b-[\Delta7\text{-His}]_2$ maquette midpoint potential was evaluated for comparison to heme $b-[H10A24]_2$. As shown in Figure 2A, as the pH value is lowered to <8.0, the E_m value of heme $b-[\Delta7\text{-His}]_2$ shows a positive increase in potential and, at pH values of <7.0, requires long equilibration times, 20 min per potential poise, to prevent hysteresis between the oxidative and reductive titrations. A +183 mV (4.2 kcal/mol) positive shift in the heme reduction potential is observed upon going from pH 8.0 (−222 mV) to pH 4.0 (−39 mV) for the heme $b-[\Delta7\text{-His}]_2$ maquette. The data show a slope of 120 mV per pH unit which indicates a $2H^+/1e^-$ proton-coupled electron transfer reaction stoichiometry. Attempts to fit the data to a $1H^+/1e^-$ redox event yielded unsatisfactory results as shown by the dotted line in Figure 2A. Fitting the pH dependence of the E_m value to a two-proton/one-electron equilibrium model, eq 2 (solid line in Figure 2A), yields a pK_a^{ox} value of 5.4 and a pK_a^{red} value of 6.8. These pK_a^{ox} and pK_a^{red} values are in the general range observed for other de novo designed heme maquettes, e.g., 4.2 and 7.0 for $[H10A24]_2$ and <4.7 and 6.8 for HP-1, respectively, which are often interpreted as an electrostatic response mechanism via glutamic acid on the basis of their assignment as such in heme $b-[H10A24]_2$ (*20*, *56*).

An alternative explanation for the data is provided by a fit to the Henderson−Hasselbalch equation (eq 3), which indicates a ligand loss mechanism of proton coupling to electron transfer. In this interpretation, reduction of ferric heme $b-[\Delta7\text{-His}]_2$ leads to protonation of the histidine residues with dissociation of the ferrous heme from the axial ligands and is described by the value of the reduced state effective proton dissociation constant, $pK_a^{eff\text{-}red}$. As shown by the bold line fit in Figure 2B, the pH dependence of the midpoint potential of heme $b-[\Delta7\text{-His}]_2$ can be fit to this model with a $pK_a^{eff-red}$ value of 6.1. These data indicate that the pK_a^{His} value, the histidine pK_a in the apo scaffold, is at least greater than 6.1 since binding of ligand to the metal lowers the ligand pK_a value, i.e., $pK_a^{eff} < pK_a$.

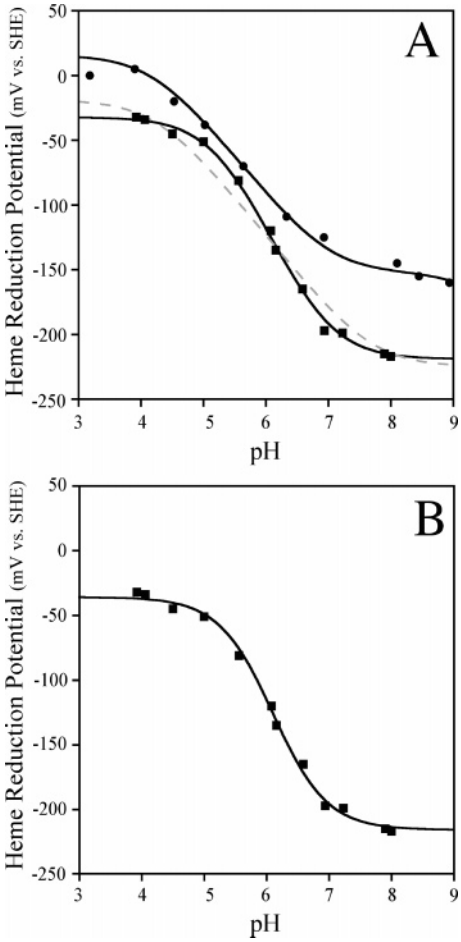

FIGURE 2: Comparison of the Pourbaix diagram of heme $b-[\Delta7\text{-His}]_2$ (■) with that of heme $b-[H10A24]_2$ (●) between pH 3.0 and 9.0. Each point represents the midpoint potential derived from a separate redox titration of the heme protein maquette. (A) The data for of heme $b-[\Delta7\text{-His}]_2$ can be fit to $2H^+/1e^-$ coupled event with pK_a^{ox} and pK_a^{red} values of 5.4 and 6.8, respectively, using eq 2 (—). A $1H^+/1e^-$ Pourbaix equation is inadequate for describing the data as shown by the dashed line. (B) The data are also adequately fit to a Henderson−Hasselbalch equation with a single two-proton $pK_a^{eff-red}$ value of 6.1 (—).

Comparison of the pH Stabilities of Heme b−[Δ7-His]₂ and Heme b−[H10A24]₂. Potentiometric pH Titrations. Panels A and B of Figure 3 show the optical spectra of ferric (thin line) and ferrous (thick line) heme $b-[\Delta7\text{-His}]_2$ at pH 8.0 and 5.3, respectively. The spectra of heme $b-[\Delta7\text{-His}]_2$ at pH 8.0 are comparable to those of heme $b-[H10A24]_2$ at pH 8.0 and 5.3, shown in panels C and D of Figure 3, respectively. Figure 3B shows that the Soret band intensity of ferrous heme $b-[\Delta7\text{-His}]_2$ is weaker than the corresponding Soret band intensities of ferric heme at the same pH value and ferrous heme at pH 8.0. These data are consistent with either dissociation of one ligand to form a five-coordinate heme protein, e.g., myoglobin, or dissociation of both ligands from the heme iron at the lower pH value (*57*).

Since the slope of the transition in pH competition experiments can be used to discriminate between loss of one ligand and loss of both ligands, potentiometric pH titrations were performed for each protein in both heme oxidation

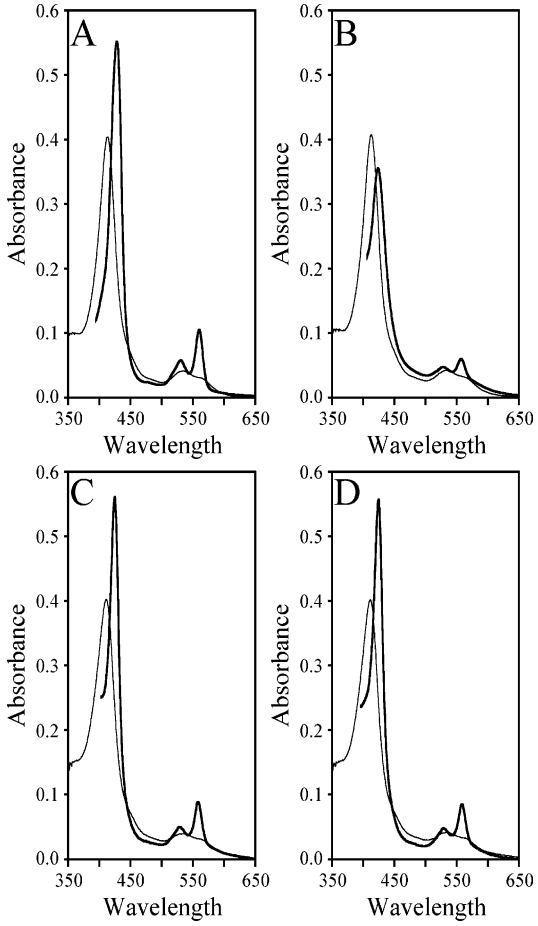

FIGURE 3: Optical spectra of oxidized (thin line) and reduced (thick line) heme $b-[\Delta 7\text{-His}]_2$ and heme $b-[\text{H10A24}]_2$ at pH 8.0 and 5.3. The lower Soret absorbance of reduced heme $b-[\Delta 7\text{-His}]_2$ at pH 5.3 (B) relative to that at pH 8.0 (A) is evidence of dissociation of heme from the axial histidine ligands. The optical spectra of heme $b-[\text{H10A24}]_2$ at pH 8.0 (C) and pH 5.3 (D) are identical. All samples were 2.0 μM heme protein and were allowed to equilibrate for 60 min prior to measurement.

states. These experiments evaluate the speciation of heme $b-[\Delta 7\text{-His}]_2$ and heme $b-[\text{H10A24}]_2$ and determine their stabilities with respect to acid. Figure 4A shows the potentiometric titrations of the heme $b-[\Delta 7\text{-His}]_2$ maquette in the oxidized and reduced states which were used to derive their respective $pK_a^{\text{eff}-\text{ox}}$ and $pK_a^{\text{eff}-\text{red}}$ values. In the oxidized state, the optical data from heme $b-[\Delta 7\text{-His}]_2$ are best fit using eq 4 to a cooperative two-proton transition with a $pK_a^{\text{eff}-\text{ox}}$ value of 2.6 as listed in Table 1. The corresponding data for the reduced state of heme $b-[\Delta 7\text{-His}]_2$ give a $pK_a^{\text{eff}-\text{red}}$ value of 5.7 when fit to a cooperative two-proton event, indicating that the lower Soret intensity observed for this maquette at pH 5.3 is due to dissociation of both histidine ligands and not formation of a stable monohistidine ligated ferrous heme protein. The higher concentration of protons required to protonate the His ligands with the ferric heme *b* bound indicates that the histidine contribution to the $[\Delta 7\text{-His}]_2$ maquette affinity for ferric heme is 1000-fold, or 4.1 kcal/mol, tighter than for ferrous heme *b* at pH values above pK_a^{His}. This result agrees, within a 2.5-fold or 0.5 kcal/mol experimental error, with the measured 300-fold difference between the heme $b-[\Delta 7\text{-His}]_2$ $K_{d1}^{\text{Fe(III)}}$ and $K_{d1}^{\text{Fe(II)}}$ values at pH 8.0 of 140 pM and 42 nM, respectively (*29*).

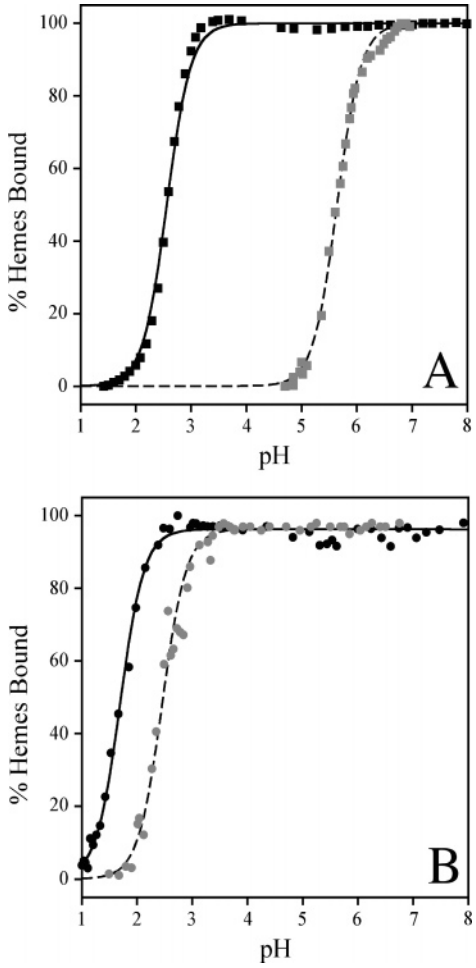

FIGURE 4: Comparison of the ferric and ferrous heme $b-[\Delta 7\text{-His}]_2$ (■) and heme $b-[\text{H10A24}]_2$ (●) heme−protein maquette stabilities derived from potentiometric titrations. The data for the oxidized (black points with solid lines) and reduced (gray points with dashed lines) heme proteins are fit to a model for the protonation of the two axial histidine residues at pK_a^{eff} for each oxidation state. (A) Fitting the data to eq 4 yields a $pK_a^{\text{eff}-\text{ox}}$ value of 2.6 and a $pK_a^{\text{eff}-\text{red}}$ value of 5.7 for ferric and ferrous heme $b-[\Delta 7\text{-His}]_2$. (B) Fits of the heme $b-[\text{H10A24}]_2$ data show $pK_a^{\text{eff}-\text{ox}}$ and $pK_a^{\text{eff}-\text{red}}$ values of 1.7 and 2.5, respectively.

In terms of the interpretation of the pH dependence of the midpoint reduction potential data in panels A and B of Figure 2, the observed $pK_a^{\text{eff}-\text{red}}$ value of 5.7 can be used to differentiate between the two models that are discussed. The coincidence of the two $pK_a^{\text{eff}-\text{red}}$ values, 5.7 and 6.1, and the improvement in the Pourbaix diagram fit using eq 3 over eq 2 indicate that the observed pH dependence of the E_m value is due to the ligating histidine residues rather than the deprotonation of local glutamic acid residues. The difference in the $pK_a^{\text{eff}-\text{red}}$ values determined using direct proton titration, 5.7, and the pH dependence of the midpoint potential, 6.1, is within the experimental error of the individual reduction potential measurements. Thus, reduction of ferric heme $b-[\Delta 7\text{-His}]_2$ leads to loss of histidine coordination at pH <7.0 and a positive shift in the E_m value. This conclusion is also supported by the observation that the ferrous heme *b* Soret band is lower in intensity than the oxidized heme *b* Soret band at pH 5.3, as shown in Figure 3B, due to loss of both axial histidine ligands from the ferrous heme.

Table 1: Thermodynamic Parameters for Heme $b-[\Delta 7\text{-His}]_2$ and Heme $b-[H10A24]_2$

		$[\Delta 7\text{-His}]_2$	$[H10A24]_2$
apoprotein	pK_a^{His}	6.7	3.0
	pK_a^{Glu}		8.0
	pK_a^{Lys}		12.0[b]
ferric heme *b*	pK_a^{eff-ox}	2.6	1.7
	pK_a^{ox} (Glu)		5.0
	pK_a^{ox} (Lys)		9.4
	K_d (pH 1.0)	21 mM[a]	13 μM[a]
	K_d (pH 5.5)	40 nM	16 nM
	K_d (pH 9.0)	140 pM[a]	32 pM[a]
ferrous heme *b*	$pK_a^{eff-red}$	5.7	2.5
	pK_a^{red} (Glu)		7.0
	pK_a^{red} (Lys)		10.3
	K_d (pH 1.0)	4.0 μM[a]	170 μM
	K_d (pH 5.5)	2.0 μM	20 nM
	K_d (pH 9.0)	37 nM[a]	1.9 nM[a]

[a] Estimated on the basis of fits to the K_d vs pH data. [b] Estimate.

As shown in Figure 4B, heme $b-[H10A24]_2$ is more resistant to histidine protonation than heme $b-[\Delta 7\text{-His}]_2$ in both the oxidized and reduced states. The potentiometric titration of ferric heme $b-[H10A24]_2$ is best fit to an equation for a cooperative two-proton transition with a pK_a^{eff-ox} value of 1.7. The optical spectra for the reduced state can be fit to the same model and give a $pK_a^{eff-red}$ value of 2.5. Since both the pK_a^{eff-ox} and $pK_a^{eff-red}$ values listed in Table 1 are significantly lower than the pK_a^{red} and pK_a^{ox} values from the reported heme $b-[H10A24]_2$ Pourbaix diagram, histidine protonation and heme loss are not involved in the observed modulation of the E_m value at pH >4.0. In addition, the lower pK_a^{eff-ox} value of the two histidines demonstrates that the histidine contribution to heme $b-[H10A24]_2$ stability is 6.3-fold, or 1.1 kcal/mol, tighter for ferric than ferrous heme *b* per histidine ligand. Thus, bis-His coordination contributes 2.2 kcal/mol greater stability to ferric heme $b-[H10A24]_2$ than to ferrous.

Ferric/Ferrous Heme b Affinity Studies. Conditional Dissociation Constant Measurements. As the heme reduction potential is governed by the ratio of the conditional dissociation constants for ferric and ferrous heme, the absolute ferric and ferrous heme affinities were determined as a function of pH in an attempt to investigate the different redox-Bohr effects observed for heme $b-[\Delta 7\text{-His}]_2$ and heme $b-[H10A24]_2$ (*39*). Figure 5 shows representative determinations of the conditional dissociation constants of ferric and ferrous heme $b-[\Delta 7\text{-His}]_2$ at pH 5.5 whose values are listed in Table 1. The ferric and ferrous heme binding isotherms shown in Figure 5 yield conditional $K_d^{Fe(III)}$ and $K_d^{Fe(II)}$ values of 40 nM and 2.0 μM for ferric and ferrous heme $b-[\Delta 7\text{-His}]_2$, respectively, at pH 5.5. A comparison of these data at pH 5.5 with those reported at pH 8.0 demonstrates that the scaffold response to pH results in differences not only in the absolute values of $K_d^{Fe(III)}$ and $K_d^{Fe(II)}$ but also in their relative values (*29*).

Figure 6 shows the conditional dissociation constants of ferric and ferrous heme $b-[\Delta 7\text{-His}]_2$ measured as a function of pH between pH 4.0 and 8.0. The data show that both the oxidized and reduced conditional dissociation constant values are attenuated at pH <7.0. The onset of the attenuation demonstrates that the proton dissociation constants of the His residues in the apo maquette, pK_a^{His}, are below 7.0. The slope of these curves, i.e., 2, represents the number of protons

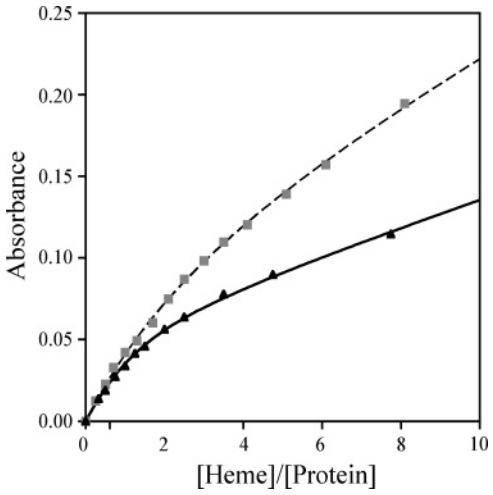

FIGURE 5: Analysis of the affinity of $[\Delta 7\text{-His}]_2$ for heme *b* in the ferric and ferrous states at pH 5.5 performed using optical spectroscopy. Titration of ferric heme *b* into a 50 nM $[\Delta 7\text{-His}]_2$ solution at pH 5.5 in a 10 cm quartz cell results in an increase in absorption at 412 nm (▲) that is fit to an equation for a 1:1 heme $b-[\Delta 7\text{-His}]_2$ complex with a heme dissociation constant of 40 nM. Ferrous heme *b* titrated into a 1 μM $[\Delta 7\text{-His}]_2$ solution at pH 5.5 in a 1.0 cm quartz cell under anaerobic conditions yields an increase in absorption at 427 nm (gray squares) which is fit to a 1:1 heme $b-[\Delta 7\text{-His}]_2$ complex with a dissociation constant of 1.9 μM, as shown by the dashed line. All samples were in 20 mM MES, 100 mM KCl, pH 5.5 buffer and allowed to equilibrate for 1 h prior to measurement on a Cary 100 spectrophotometer.

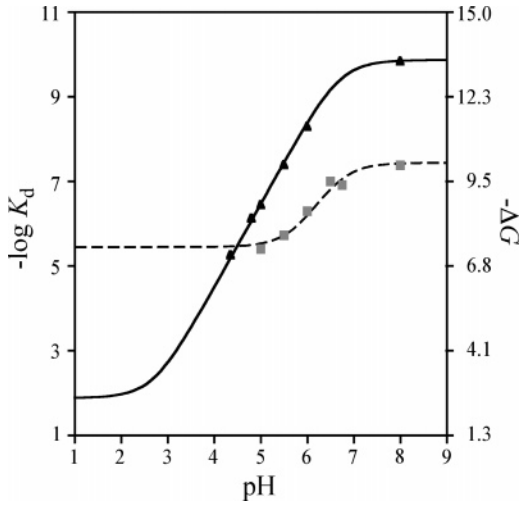

FIGURE 6: Evaluation of the conditional dissociation constants of ferric and ferrous heme $b-[\Delta 7\text{-His}]_2$ over the pH range of 1.0–8.0. Each point represents an individual determination of the $K_d^{Fe(III)}$ (▲) or $K_d^{Fe(II)}$ (gray squares) values as shown in Figure 5 for pH 5.5. The data are fit to eq 9 on the basis of a model in which the conditional dissociation constants are modulated by protonation of the two histidine residues with pK_a^{eff-ox} and $pK_a^{eff-red}$ values of 2.6 and 5.6, respectively, and an apoprotein pK_a^{His} value of 6.7.

in competition with heme binding which is demonstrative of bis-His heme coordination with the measured pK_a^{eff-ox} and $pK_a^{eff-red}$ values.

At pH values significantly above pK_a^{His}, where histidine protonation becomes negligible, the maximal affinity of this peptide scaffold for ferrous and ferric heme is observed. At pH 8.0, $K_{d1}^{Fe(III)}$ and $K_{d1}^{Fe(II)}$ values of 42 nM and 140 pM, respectively, have been determined which indicate a 300-fold, or 3.4 kcal/mol, difference between the affinity of the peptide for ferric and ferrous heme that is also reflected in

the measured pK_a^{eff-ox} and $pK_a^{eff-red}$ values of 2.6 and 5.7, respectively. At pH values approaching or below pK_a^{His}, the conditional K_d values are seen to weaken due to proton competition with a slope of two $-\log K_d$ units per pH unit, as shown in Figure 6. This continues until the pH reaches the pK_a^{eff-ox} and $pK_a^{eff-red}$ values, the point at low pH where the curves become pH-independent. Below the pK_a^{eff} values, pH no longer modulates the oxidized or reduced heme affinity as the heme iron does not coordinate to the protonated His residues, $HisH^+$. While the heme iron is not ligated by $HisH^+$, the porphyrin remains associated with the protein scaffold as evidenced by the association constant values at pH 1.0.

The reduced heme data in Figure 6 are fit to an equilibrium model based on histidine protonation using the measured $pK_a^{eff-red}$ value of 5.7 along with a pK_a^{His} value and the formation constant for ferrous heme *b* binding, K_f^{red}. The fit yields an apoprotein pK_a^{His} value of 6.7, the onset of pH dependence, and levels out at high pH at a K_f^{red} value of $2.7 \times 10^7\ M^{-1}$. This formation constant represents a dissociation constant value of 37 nM at high pH, consistent with the value of 42 nM measured at pH 8.0, and demonstrates that binding of ferrous heme to this maquette is favorable by 10.1 kcal/mol. At low pH, the fit levels out at a $K_f^{assoc-red}$ value of $2.8 \times 10^5\ M^{-1}$ which indicates that association of ferrous heme *b* with the hydrophobic core of $[\Delta7\text{-His}]_2$ is favorable by 7.4 kcal/mol. Thus, the affinity of $[\Delta7\text{-His}]_2$ for reduced heme *b* at pH 8.0, $2.4 \times 10^7\ M^{-1}$, is due mostly to association of the porphyrin with the peptide, with an only 2.7 kcal/mol contribution from histidine ligation.

The fit to the corresponding ferric heme $b-[\Delta7\text{-His}]_2$ data includes the pK_a^{eff-ox} value of 2.6 measured by potentiometric titration and the apoprotein pK_a^{His} value of 6.7 as expected on the basis of the ferrous results and yields a K_f^{ox} value of $7.4 \times 10^9\ M^{-1}$ at high pH values. This K_f^{ox} value represents a dissociation constant of 135 pM and a free energy of binding of -13.5 kcal/mol. In comparison to natural protein scaffolds, the maquette $K_d^{Fe(III)}$ of 135 pM is tighter than the value of 9 nM for ferric cyt b_{562} and weaker than the value of 10 fM for metmyoglobin (*40*, *50*). In addition, the fit gives a ferric heme−protein hydrophobic core association constant, $K_f^{assoc-ox}$, of $4.8 \times 10^1\ M^{-1}$ (2.3 kcal/mol) that shows ferric heme *b* has a weaker association with the protein core than ferrous heme *b*. In contrast to the ferrous results, the data show that histidine ligation is dominant in the overall formation constant of ferric heme $b-[\Delta7\text{-His}]_2$ as it contributes 11.2 kcal/mol to the overall affinity of 13.5 kcal/mol. These results are consistent with the observation from iron porphyrin model complexes that bis-imidazole sites preferentially bind ferric heme over ferrous, and from heme proteins that burial of a formally charged ferric porphyrin core, $[Fe^{III}(por^{2-})]^+$, in a low-dielectric hydrophobic core is energetically unfavorable compared to burial of a formally neutral ferrous porphyrin core, $[Fe^{II}(por^{2-})]^0$ (*58*−*60*).

The fits to the K_d versus pH data can be used to determine the mechanistic basis for the Pourbaix diagram given in Figure 2B. The pH dependence of the midpoint reduction potential of heme $b-[\Delta7\text{-His}]_2$ observed between pH 8.0 and 4.0 is due to the absolute destabilization of the ferric state, or mechanism B of Scheme 1. Once the solution pH is below the ferrous heme $b-[\Delta7\text{-His}]_2$ $pK_a^{eff-red}$ value of 5.7, the ferrous K_d value is constant because the histidines are not coordinated to the ferrous ion. In other words, the positive shift in E_m as the pH value is lowered is due solely to destabilization of the ferric state in $[\Delta7\text{-His}]_2$ as the stability of ferrous heme $b-[\Delta7\text{-His}]_2$ has been fully compromised by protons. Coincidentally, the affinities of $[\Delta7\text{-His}]_2$ for ferric and ferrous heme *b* are equivalent at a pH value of 4.5 where the midpoint reduction potential is -38 mV. Since the $K_d^{Fe(III)}/K_d^{Fe(II)}$ ratio is unity at this pH, the measured value of E_m^{bound} equals that of E_m^{free}. Thus, at this pH value, the binding contribution of axial histidine ligands in ferric heme $b-[\Delta7\text{-His}]_2$ has exactly compensated for the difference between association of ferric and ferrous porphyrin with the peptide.

While the bulk of the changes observed in Figure 2B are due to dissociation of histidine from the heme iron upon reduction, the dissociation of the ferric heme from the protein scaffold also influences the Pourbaix diagram. At pH values approaching the pK_a^{eff-ox} value of 2.6, the electrochemical event changes to the midpoint potential of heme associated with the protein scaffold, but not coordinated to the histidine ligands. At this point, the low pH ratio of the ferric and ferrous K_d values predicts an E_m value of $+144$ mV (vide supra) which is similar to the value of $+100$ mV observed for four-coordinate heme c_i in the cytochrome b_6f complex (*61*, *62*). This is the value at which the Pourbaix diagram in Figure 2B would level out if the E_m measurements were taken at concentrations sufficient to keep the heme associated with the peptide in both oxidation states. However, the measurement of the E_m values at micromolar concentrations leads to the observed plateau at -38 mV due to the dissociation of ferric heme from the protein scaffold under these conditions. Thus, the dissociation of the ferric heme from the maquette scaffold at low pH also influences the observed Pourbaix diagram.

For the $[H10A24]_2$ maquette scaffold, conditional dissociation constants of ferric and ferrous heme *b* were determined over the pH range of 1.5−7.0. Figure 7 shows representative ferric and ferrous K_d determinations at pH 5.5 which yield conditional $K_d^{Fe(III)}$ and $K_d^{Fe(II)}$ values of 16 and 20 nM, respectively. Thus, the measured $K_d^{Fe(III)}$ and $K_d^{Fe(II)}$ values of heme $b-[H10A24]_2$ are virtually identical at pH 5.5.

The conditional dissociation constants of ferric and ferrous heme $b-[H10A24]_2$ as a function of pH are shown in Figure 8. These data are best fit to an equilibrium model in which the attenuation in the conditional K_d values is due to the protonation of three residues: the two histidine ligands and the glutamate residue involved in the redox-Bohr effect. A $K_d^{Fe(II)}$ value of 1.9 nM can be extrapolated from the curve fit at pH 9.0, above the pK_a^{His} and pK_a^{red} values, where the histidines are formally neutral and the glutamate is deprotonated. As the pH is lowered to near 7.0, the pK_a^{red} value, the glutamate involved in the redox-Bohr effect becomes protonated and the $K_d^{Fe(II)}$ values are weakened slightly. Between pH 7.0 and 4.0, the measured $K_d^{Fe(II)}$ values are constant within error, as the glutamic acid and histidine residues are formally neutral with and without ferrous heme bound. Below pH 4.0, the histidines begin to protonate in the apoprotein scaffold which weakens the observed conditional $K_d^{Fe(II)}$ values, consistent with the independently measured $pK_a^{eff-red}$ value of 2.5. The fit to the ferrous heme $b-[H10A24]_2$ $K_d^{Fe(II)}$ data in Figure 8 uses the independently

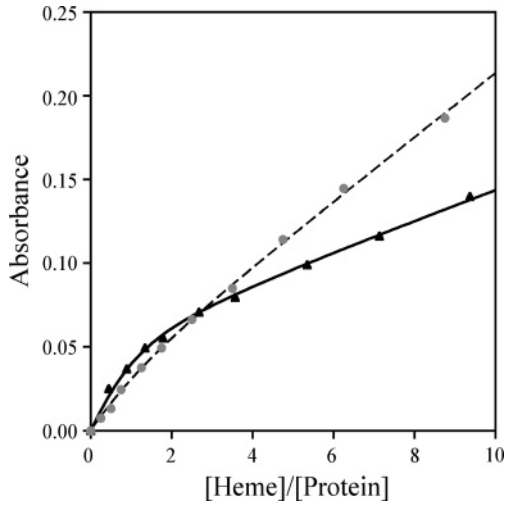

FIGURE 7: Thermodynamic analysis of the affinity of $[H10H24]_2$ for ferric and ferrous heme *b* at pH 5.5 followed by optical spectroscopy. Ferric heme *b* was titrated into a 50 nM solution of $[H10A24]_2$ in 20 mM MES, 100 mM KCl, pH 5.5 buffer in a 10 cm quartz cell. The titration yields in increase in the absorption at 412 nm (▲) whose fit to a 1:1 heme *b*−$[H10A24]_2$ complex binding model with a $K_d^{Fe(III)}$ value of 16 nM is shown with a solid line. Ferrous heme *b* was titrated into a 30 nM $[H10A24]_2$ solution in a 10 cm quartz cell under anaerobic conditions. The absorption at 426 nm (gray circles) is fit (dotted line) to a 1:1 heme *b*−$[H10A24]_2$ complex model with a $K_d^{Fe(II)}$ of 20 nM. All samples were equilibrated overnight prior to measurement.

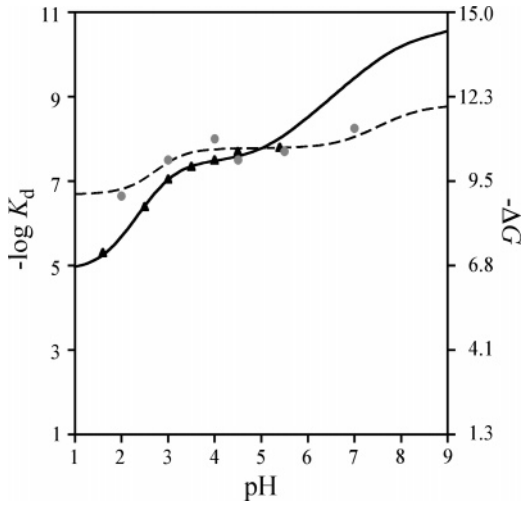

FIGURE 8: Evaluation of the conditional dissociation constants for heme *b*−$[H10A24]_2$ over the pH range of 1.0−8.0. Each point represents an individual determination of the $K_d^{Fe(III)}$ (▲) or $K_d^{Fe(II)}$ (gray circles) values as shown in Figure 7 for pH 5.5. The data are fit to eq 8 on the basis of a model in which the conditional dissociation constants are modulated by protonation of the two histidines (pK_a^{eff-ox} and $pK_a^{eff-red}$ values of 1.7 and 2.5, respectively, and an apoprotein pK_a^{His} value of 3.0), a glutamic acid (pK_a^{ox}, pK_a^{red}, and pK_a^{Glu} values of 5.0, 7.0, and 8.0, respectively), and a lysine residue (pK_a^{ox}, pK_a^{red}, and pK_a^{Lys} values of 9.4, 10.3, and 12.0, respectively).

measured $pK_a^{eff-red}$ (His) and pK_a^{red} (Glu) values of 2.5 and 7.0, respectively, and yields proton dissociation constant values for the apoprotein histidine and glutamic acid residues, pK_a^{His} and pK_a^{Glu}, of 3.0 and 8.0, respectively. With regard to pK_a^{His}, the value of 2.5 is lower than the pK_a^{His} value of 5.4 measured in a related and structurally characterized apo maquette scaffold and close to the value of ~3.5 measured for the noncoordinating His26 in tuna cytochrome *c* (*63*−*65*). This value of 2.5 suggests that the histidine residues are well-buried in a hydrophobic core, as multiconformation continuum electrostatics calculations show that burial can shift the pK_a value by 3−5 units (*7*). With regard to the pK_a^{Glu} value of 8.0, our assignment is based on the observation that repeated attempts to measure the K_d at pH 8.0 resulted in tight binding curves indicative of a subnanomolar K_d value at pH 8.0. Since the K_d value of 10 nM at pH 7.0 could be measured, the tighter conditional dissociation constant at pH 8.0 necessitated a pK_a^{Glu} value of 8.0 to fit the data in Figure 8 using the minimal equilibrium model presented in eq 5. Since Shifman et al. had previously assigned the pK_a^{red} (Glu) value of 7.0 on the basis of the Pourbaix diagram, our assignment of the $pK_a = 8.0$ species to the apoprotein Glu residue is reasonable, although it may not be a unique solution as it is possible that the $pK_a = 8.0$ species is another ionizable group.

The fit at low pH shows that ferrous heme *b* partitions into the hydrophobic core of $[H10A24]_2$ with a $-\Delta G^{assoc-red}$ value of 9.2 kcal/mol, a $K_f^{assoc-red}$ of 5.8×10^6 M^{-1}, that is 1.8 kcal/mol tighter than the corresponding value from ferrous heme *b*−$[\Delta 7\text{-His}]_2$. The coordination of the histidine residues above $pK_a^{eff-red}$ and the deprotonation of the glutamic acid at pK_a^{red} each contribute an additional 1.4 kcal/mol to the heme *b* affinity. The heme *b*−$[H10A24]_2$ $K_d^{Fe(II)}$ value at pH 9.0 is 1.9 nM, or 11.9 kcal/mol. Thus, ferrous heme affinity in $[H10A24]_2$ is a combination of porphyrin−protein hydrophobic interactions, axial ligand coordination, and glutamic acid deprotonation with the bulk being contributed by porphyrin−protein hydrophobic interactions, 9.2 kcal/mol of the 11.9 kcal/mol at pH 9.0.

The data for ferric heme *b*−$[H10A24]_2$ also show the influence of three ionizable groups. At pH values above the apoprotein pK_a^{His} and pK_a^{Glu} values, pH >8.0, where the histidines are formally neutral and the glutamate is deprotonated, $K_d^{Fe(III)}$ values too tight to be determined using optical spectroscopy are observed. As the pH is lowered, the fit indicates that the glutamate becomes protonated and the $K_d^{Fe(III)}$ values are weakened because the stabilizing electrostatic interaction between the anionic glutamate and the cationic ferric heme *b* porphyrin core is lost. Below pH 4.0, the conditional $K_d^{Fe(III)}$ values weaken further due to the competition between histidine protonation and histidine coordination to the heme iron which has a pK_a^{eff-ox} value of 1.7. The fit to the $K_d^{Fe(III)}$ data in Figure 8 uses the independently measured pK_a^{eff-ox} (His) value and yields a value of 5.0 for pK_a^{ox} (Glu) along with the same proton dissociation constant values for the apoprotein histidine and glutamic acid residues, a pK_a^{His} of 3.0 and a pK_a^{Glu} of 8.0, observed in the reduced heme *b* data fit. This analysis places a value of 5.0 on the oxidized glutamate pK_a^{ox} value rather than the value of 4.2 previously reported from the Pourbaix diagram (*20*). This 1.1 kcal/mol discrepancy is due to a small amount of ferrous heme *b* dissociation at pH <4.0 resulting from the pK_a^{eff} (His) value of 2.5 which was not included in the original Pourbaix fit.

In contrast to the results from ferric heme *b*−$[\Delta 7\text{-His}]_2$, the $K_d^{Fe(III)}$ versus pH data for heme *b*−$[H10A24]_2$ indicate that histidine ligation is the smallest contributor to ferric heme affinity. Histidine ligation provides only 3.6 kcal/mol to heme affinity which when combined with the value of 6.7 kcal/mol due to porphyrin−protein hydrophobic interac-

tions, a $K_f^{assoc-ox}$ of 7.9×10^4 M^{-1}, and 4.1 kcal/mol in electrostatic stabilization by the glutamate residue yields the $K_d^{Fe(III)}$ value of 32 pM at pH 9.0 (14.4 kcal/mol). The minor contribution of metal−ligand coordination to this bundle is consistent with the observation that similar bundles without His ligands also associate with ferric heme (*66*). Despite the differences in their contributions to ferric heme *b* affinity revealed by this analysis, $[\Delta 7\text{-His}]_2$ and $[H10A24]_2$ possess similar dissociation constants at pH 9.0, 140 and 32 pM, respectively.

In terms of proton-coupled electron transfer, the mechanistic basis for the observed pH dependence of the midpoint reduction potential of heme *b*−$[H10A24]_2$ is the continued destabilization of ferric heme *b*−$[H10A24]_2$ with the decrease in pH from 7.0 to 5.0. Over this pH range, the $K_d^{Fe(II)}$ values are constant while the $K_d^{Fe(III)}$ values continue to weaken. Thus, the destabilization of ferric heme *b*−$[H10A24]_2$ due to glutamate protonation accounts for the observed modulation in the E_m values with pH reported by Shifman et al. (*20*). At pH <4.0, the heme begins to dissociate from the axial ligands upon reduction which influences the Pourbaix diagram observed at micromolar protein concentrations similar to the findings for heme *b*−$[\Delta 7\text{-His}]_2$. Coincidentally, the stabilities of ferric and ferrous heme *b*−$[H10A24]_2$ are equivalent at pH 5.0 where the midpoint reduction potential is measured as −38 mV. A comparison of the E_m values for each scaffold where the ratio of their $K_d^{Fe(III)}$ and $K_d^{Fe(II)}$ values is 1.0, and $E_m^{bound} = E_m^{free}$, demonstrates that both are −38 mV which validates our thermodynamic analysis on the basis of eq 7. Furthermore, while the relative ratios are identical when their reduction potentials are −38 mV, the absolute values of $K_d^{Fe(III)}$ and $K_d^{Fe(II)}$ are different.

DISCUSSION

Two related heme protein maquettes have been utilized in evaluating the role of the protein scaffold and its response to pH in modulating the electrochemical activity of bound heme *b*. The data at pH 8.0 illustrate that the $[H10A24]_2$ scaffold binds both oxidized and reduced heme *b* tighter than $[\Delta 7\text{-His}]_2$. This leads, within error, to the observed 66 mV positive shift in the heme reduction potential between these scaffolds at pH 8.0 via mechanism D of Scheme 1. In terms of solution pH, analysis of the Pourbaix diagram of heme *b*−$[\Delta 7\text{-His}]_2$ shows that it exhibits a $2H^+/1e^-$ coupled event, as compared with the two distinct $1H^+/1e^-$ events in heme *b*−$[H10A24]_2$. Detailed analysis of the heme binding thermodynamics of both of these proton-coupled electron transfer events demonstrates that the mechanisms and the sites of proton coupling are distinct. Furthermore, the data allow the individual contributions of porphyrin−protein hydrophobic interactions, histidine coordination, and electrostatic interactions between the heme and the scaffold to be quantified, which thereby reveals the effects of each protonation event on the absolute affinity of these scaffolds for ferric and ferrous heme *b*.

While atomic detail structures of heme *b*−$[H10A24]_2$ and heme *b*−$[\Delta 7\text{-His}]_2$ are not available, several lines of evidence indicate that the heme is more effectively sequestered from solvent in heme *b*−$[H10A24]_2$. First, the histidine ligands in apo-$[H10A24]_2$ are more acidic than those in apo-$[\Delta 7\text{-His}]_2$ as evidenced by their respective pK_a^{His} values of 3.0 and 6.7. Second, the more positive reduction potential of heme *b*−$[H10A24]_2$ relative to heme *b*−$[\Delta 7\text{-His}]_2$ is consistent with the difficulty in burying the formally charged porphyrin macrocycle of ferric heme *b*, i.e., $[Fe^{III}(por^{2-})]^+$, within a low-dielectric hydrophobic core (*58*−*60*). Third, the extrapolated association constant, K_f^{assoc}, values at pH 1.0, where the histidines are protonated and do not coordinate the heme iron, indicate greater affinity for each oxidation state of heme *b*−$[H10A24]_2$ than for heme *b*−$[\Delta 7\text{-His}]_2$ due to greater protein−porphyrin macrocycle interaction. The greater protein−porphyrin macrocycle interactions in $[H10A24]_2$ relative to $[\Delta 7\text{-His}]_2$ ultimately lead to the observed differences in their proton-coupled electron transfer mechanisms and likely reflect the molten globule nature of apo-$[H10A24]_2$, as apo-$[\Delta 7\text{-His}]_2$ is more conformationally specific (*29*).

The differences in protein−porphyrin macrocycle interactions between these two scaffolds, as evidenced by their K_f^{assoc} values, play a significant role in elevating the reduction potential values of heme *b*−$[H10A24]_2$ over those of heme *b*−$[\Delta 7\text{-His}]_2$. While stronger porphyrin−protein hydrophobic interactions lead to the expected relative destabilization of ferric heme *b* with respect to ferrous heme *b*, no firm expectations could be made on the absolute stabilization and/or destabilization of the two oxidation states. The data presented reveal that the relative stabilization of the ferrous state is mostly due to an absolute stabilization of the ferrous state binding rather than an absolute destabilization of the ferric state, as might be expected on the basis of the greater difficulty in desolvating the formally charged ferric porphyrin core (*68*). The data show that the relative stabilization of ferrous heme *b* over ferric in heme *b*−$[H10A24]_2$ compared to heme *b*−$[\Delta 7\text{-His}]_2$ is a result of the stabilization of both the ferrous and ferric oxidation states, or mechanism D in Scheme 1. Thus, stronger porphyrin−peptide hydrophobic interactions stabilize both oxidation states, but desolvation of the cationic ferric porphyrin core results in weaker stabilization of the ferric heme relative to ferrous and the positive shift in the E_m value.

It is evident from the Pourbaix diagrams in Figure 2A that the mechanisms of proton-coupled electron transfer in these two maquette scaffolds are distinct. In the case of heme *b*−$[H10A24]_2$, the site of coupling of a proton to heme oxidation/reduction is a glutamic acid residue as illustrated in Scheme 2A and as first identified by Shifman et al. (*20*). This electrostatic response mechanism shifts the E_m value to more positive potentials as the solution pH value is lowered from 8.0 to 5.0 due to the protonation of the glutamate in the ferrous state. The extrapolated $K_d^{Fe(III)}$ values show that the negatively charged glutamate interacts with the formal positive charge on the porphyrin core of ferric heme *b*, i.e., $[Fe^{III}(por^{2-})]^+$, to stabilize the ferric heme *b* by 4.1 kcal/mol. The corresponding measured $K_d^{Fe(II)}$ values exhibit an only minor stabilization, 1.4 kcal/mol, of the ferrous state, consistent with a formally neutral reduced heme core, i.e., $[Fe^{II}(por^{2-})]$. The combination of the changes in $K_d^{Fe(III)}$, due to loss of the stabilization at low pH values, and the small changes in $K_d^{Fe(II)}$ leads to the more positive heme reduction potentials at pH 5.0 relative to those at pH 8.0. Thus, the proton-coupled electron transfer event that leads to more positive reduction potentials in heme

Scheme 2: Mechanisms of Proton-Coupled Electron Transfer in the $[H10A24]_2$ and $[\Delta 7\text{-His}]_2$ Heme−Protein Maquettes

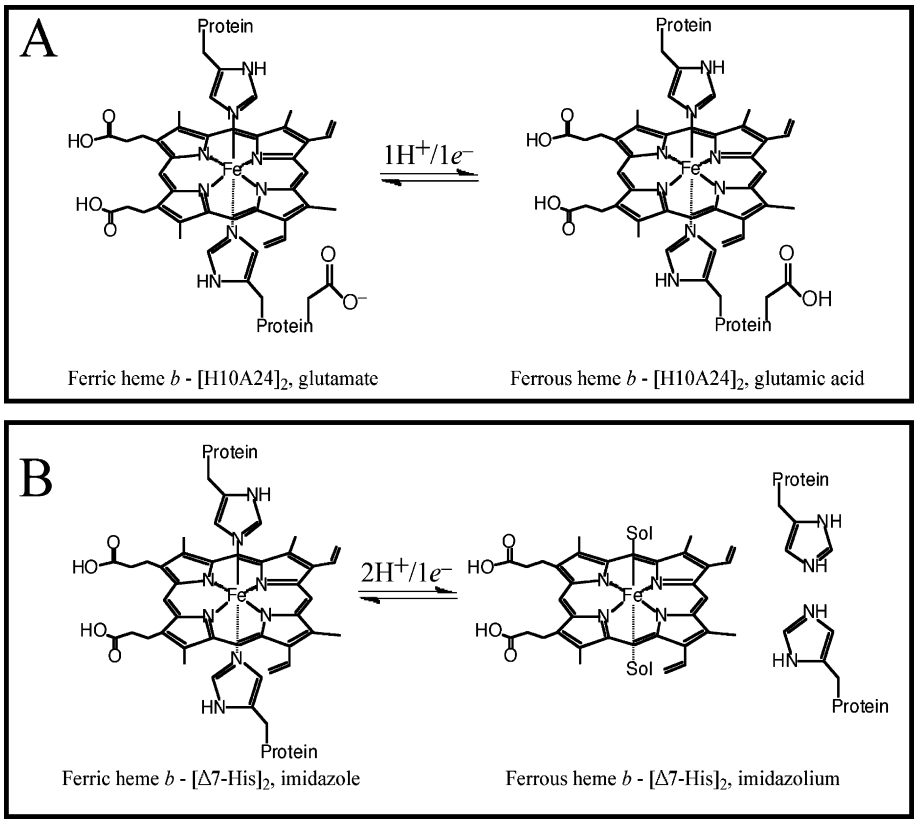

$b-[H10A24]_2$ at pH <8.0 acts via mechanism E in Scheme 1 as protonation of a glutamate residue destabilizes both ferrous and ferric heme binding (*63*).

In the case of $[\Delta 7\text{-His}]_2$, coupling of a proton to heme reduction has a stoichiometry of $2H^+/1e^-$ and is assigned to the histidine ligands to the heme iron as illustrated in Scheme 2B. Taken alone, the observed positive shift in the E_m value as the pH is lowered from 8.0 to 4.0 is consistent with an electrostatic response mechanism in which two ionizable groups in the heme protein protonate, e.g., heme propionate, lysine, glutamate, histidine, or arginine. The observed pK_a values in the $2H^+/1e^-$ fit to the Pourbaix diagram, a pK_a^{ox} of 5.4 and a pK_a^{red} of 6.8, might suggest either the protonation of a pair of glutamate residues on the basis of heme $b-[H10A24]_2$ results or the protonation of a histidine and a propionate group in analogy to published results on a $2H^+/2e^-$ event in cytochrome c_3 (*18*, *19*). However, the $pK_a^{eff-red}$ value of 5.7 identified in the ferrous potentiometric titration clearly demonstrates that the histidine residues are the site of protonation. This ligand loss mechanism is observed in cytochrome c'' and was originally proposed by Coryell and Pauling for the Bohr effect in hemoglobin, although it ultimately proved not to be the active mechanism (*69*−*71*). In the case of designed proteins, a ligand loss mechanism may also be active in other systems that exhibit possible $2H^+/1e^-$ stoichiometries, e.g., mimochrome IV and HP-1 (*22*, *56*). The dissociation of heme *b* from the protein scaffold upon reduction results in the long equilibration times required to prevent hysteresis in the electrochemistry and the weaker ferrous heme Soret band intensity relative to oxidized heme, as shown for ferrous heme $b-[\Delta 7\text{-His}]_2$ at pH 5.3. The latter is evident in other de novo designed heme proteins at pH values as high as 8.0 and may signal the presence of $2H^+/1e^-$ redox Bohr effects due to a similar ligand loss mechanism (*72*−*75*). The evaluation of the heme $b-[\Delta 7\text{-His}]_2$ conditional dissociation constants demonstrate that the redox-Bohr effect alters the ferric and ferrous heme affinities by two different mechanisms in Scheme 1. Above the $pK_a^{eff-red}$ value of 5.7, the redox-Bohr effect is due to destabilization of the ferric heme with smaller changes in the ferrous heme, or mechanism E of Scheme 1. Below the $pK_a^{eff-red}$ value of 5.7, the ferrous heme affinity of $[\Delta 7\text{-His}]_2$ is constant and the ferric heme affinity continues to drop until its pK_a^{eff-ox} value of 2.6, or mechanism B of Scheme 1.

The data in Figures 6 and 8 allow the formation constants for each heme protein maquette to be parsed into the contributions from their individual interactions which has not been possible in earlier studies on natural heme proteins (*50*, *51*). As shown in Scheme 3, the contributions of heme association with the protein scaffold, ΔG^{assoc}, and metal−ligand coordination, ΔG^{ML}, to the formation constant can be described on the basis of the data for $[\Delta 7\text{-His}]_2$. At low pH values where the histidine residues are protonated, the extrapolated fit shows that the hydrophobic core of the peptide associates with the formally neutral ferrous porphyrin core, $[Fe^{II}(por^{2-})]^0$, more tightly than the formally charged ferric porphyrin core, $[Fe^{III}(por^{2-})]^+$, i.e., −7.4 kcal/mol versus −2.3 kcal/mol, or 5.1 kcal/mol. This 5.1 kcal/mol free energy difference between ferric and ferrous heme association represents a +220 mV shift in the associated heme reduction potential relative to E_m^{free}, or the value of +144 in Scheme 3.

As the pH is increased, the contribution of the histidine ligands can be extracted from the data and its fit. In $[\Delta 7\text{-His}]_2$, the axial coordination of the heme iron contributes 11.2 and 2.7 kcal/mol to ferric and ferrous protein stability,

Scheme 3: Contributors to the Thermodynamic Affinity and Electrochemistry in the Heme $b-[\Delta 7\text{-His}]_2$ Maquette

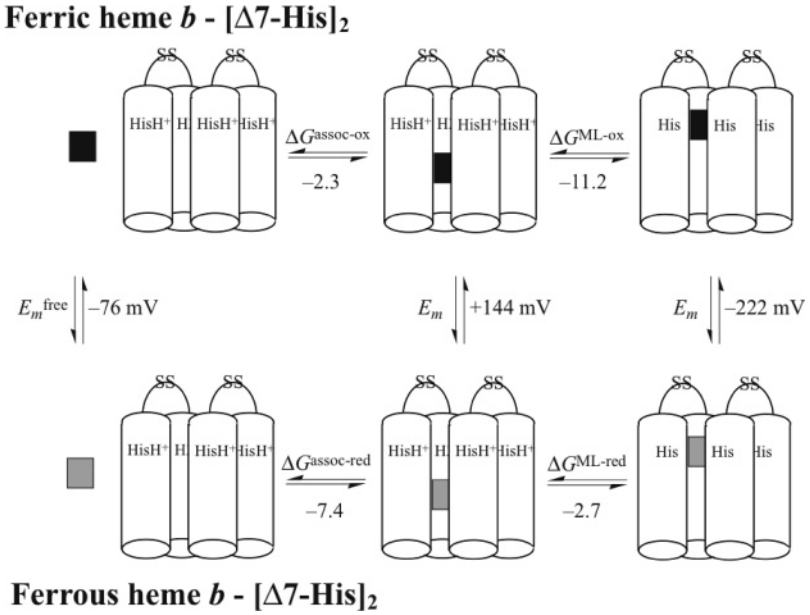

Scheme 4: Contributors to the Thermodynamic Affinity and Electrochemistry in the Heme $b-[\text{H10A24}]_2$ Maquette

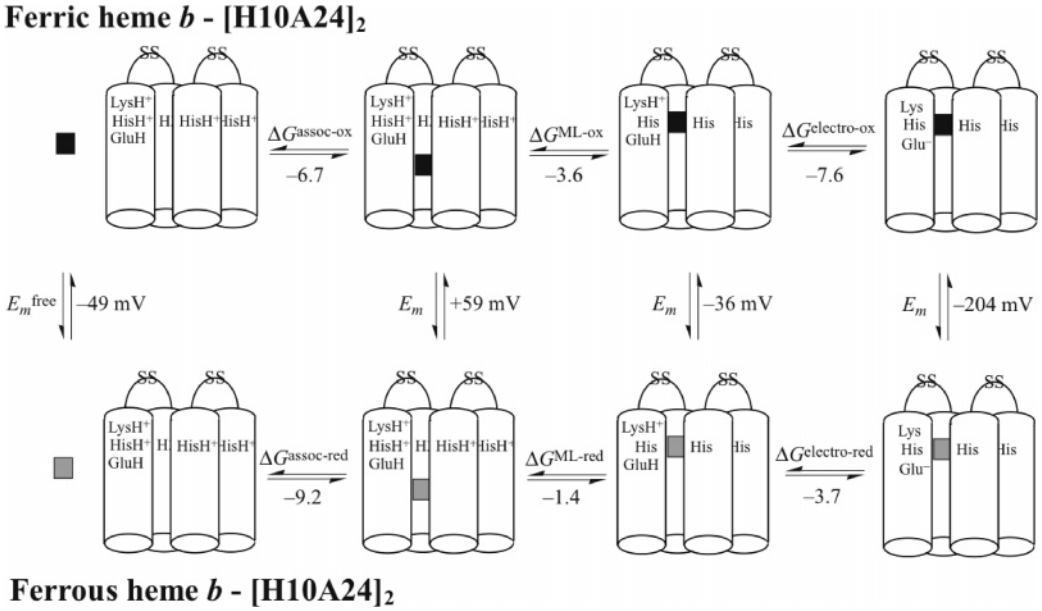

respectively. As expected on the basis of small molecule model complexes, histidine coordination contributes more to ferric stability than to ferrous (*39*). This 8.5 kcal/mol stabilization of ferric over ferrous heme by axial coordination represents a −366 mV shift in the reduction potential of the histidine-ligated heme $b-[\Delta 7\text{-His}]_2$, at pH 8.0 ($E_m = -222$ mV), versus the heme-associated heme $b-[\Delta 7\text{-His}]_2$, at pH 2.0 ($E_m = +144$ mV). Thus, axial coordination by histidine residues counteracts the positive potential shift due to porphyrin−protein hydrophobic interactions, and the sum of these two effects, +220 mV + (−366 mV), or −146 mV, equals the difference between E_m^{bound} and E_m^{free} as shown in Scheme 3. Since the reduction potential of heme $b-[\Delta 7\text{-His}]_2$ at pH 8.0 is −222 mV, the value of E_m^{free} derived from this data is −76 mV, or −222 mV − (−146 mV). This value of E_m^{free} derived from the entire data set coincides, within a 43 mV or 1.0 kcal/mol experimental error, with the value of −38 mV taken from the redox titration at pH 4.5 where the ferric and ferrous K_d values of heme $b-[\Delta 7\text{-His}]_2$ are equivalent and eq 7 reduces to $E_m^{bound} = E_m^{free}$. Heme burial and axial ligation combine, as shown in Scheme 3, to yield the observed ferric and ferrous formation constants of heme $b-[\Delta 7\text{-His}]_2$, 7.4×10^9 and 2.8×10^7 M^{-1}, respectively. However, the ferric formation constant is mostly due to axial coordination, while porphyrin association with the hydrophobic core contributes the bulk of the ferrous formation constant.

Scheme 4 shows that electrostatic effects between the heme and the protein scaffold contribute to the heme $b-[\text{H10A24}]_2$ formation constants in addition to porphyrin−protein hydrophobic interactions and axial ligation. If one starts at pH 1.0, the extrapolated fit shows that burial of ferrous heme into $[\text{H10A24}]_2$ is more favorable than burial of ferric heme by 2.5 kcal/mol, consistent with the presence of a low-dielectric hydrophobic core. In addition, the similarity of the ferric heme *b* association constant, $\Delta G^{assoc-ox}$

of −6.7 kcal/mol, to the −7.6 kcal/mol ferric state stabilization observed upon the burial of the His/Met ligated heme *c* in horse heart cytochrome *c* upon protein folding indicates that heme burial in these two scaffolds coincidentally stabilizes ferric heme to similar extents (*51*). While the difference in binding between ferrous and ferric heme is smaller in the $[H10A24]_2$ scaffold (2.5 kcal/mol) than in the $[\Delta7\text{-His}]_2$ scaffold (5.1 kcal/mol), the magnitudes of the binding energies are larger in $[H10A24]_2$ than in $[\Delta7\text{-His}]_2$. The larger magnitude of the binding energies is likely due to the ability of the more molten globular hydrophobic core in $[H10A24]_2$ to accommodate the porphyrin macrocycle as compared with $[\Delta7\text{-His}]_2$. The smaller difference in ferric and ferrous heme stabilization, 2.5 kcal/mol, represents a +108 mV shift in the reduction potential relative to E_m^{free}. While $[H10A24]_2$ has stronger protein−porphyrin macrocycle interactions than $[\Delta7\text{-His}]_2$, this does not lead to a larger reduction potential shift upon association, +108 mV versus +220 mV, because of the weak association of ferric heme with $[\Delta7\text{-His}]_2$. In either case, the E_m values of the associated hemes are close to that observed for the four-coordinate heme c_i in the cytochrome b_6f complex (*61*−*62*). At higher pH values, axial coordination of the heme iron is evident and contributes 3.6 and 1.4 kcal/mol to ferric and ferrous protein stability, respectively. This 2.2 kcal/mol stabilization of ferric over ferrous represents a −95 mV shift in the heme reduction potential relative to that for the state where heme is associated but not ligated.

For ferric and ferrous heme $b-[H10A24]_2$, there are additional electrostatic contributions to the formation constants due to the deprotonation of the glutamic acid and lysine residues, $\Delta G^{electro}$ in Scheme 4. Deprotonation of the glutamic acid responsible for the proton-coupled electron transfer event results in a relative 2.6 kcal/mol, 112 mV observed in Figure 1, stabilization of ferric over ferrous heme binding between pH 5.0 and 8.0. As shown in Figure 8, this 2.6 kcal/mol is due to a 1.4 kcal/mol stabilization of the ferrous state and a 4.1 kcal/mol stabilization of the ferric state. The anionic glutamate stabilizes the formally charged ferric porphyrin core, as expected, and the 1.4 kcal/mol stabilization of the ferrous state may be due to the better hydrophobic contact between the glutamic acid side chain and the ferrous heme. In the case of the lysine residues, the Pourbaix diagram indicates a 52 mV (1.2 kcal/mol) relative stabilization of ferric heme over ferrous heme. Using a value of 12.0 for the lysine pK_a in the apoprotein, we speculate that a combination of absolute stabilization of the ferric state by 3.5 kcal/mol and stabilization of the ferrous state by 2.3 kcal/mol is responsible for the observed 1.2 kcal/mol relative stabilization. Thus at pH 12.0, the total electrostatic stabilization of the ferric state is 7.6 kcal/mol with the ferrous state stabilized by 3.7 kcal/mol. The difference in these electrostatic stabilization terms for ferric and ferrous heme *b* indicates a −168 mV shift in reduction potential between the bis-His ligated heme states where the glutamic acid and lysine are either protonated or deprotonated. Thus, the affinities of ferric and ferrous heme *b* for $[H10A24]_2$ at pH 12, and the corresponding −204 mV potential, are due to a combination of heme association, axial coordination, and electrostatic effects from glutamate and lysine residues. These effects can be used to deduce a value of −49 mV for E_m^{free}. Since the value of E_m^{free} is expected to be scaffold-independent, the similarity of the values determined from the heme $b-[H10A24]_2$ and heme $b-[\Delta7\text{-His}]_2$ data, as well as its pH independence, validates the thermodynamics that are presented. Ultimately, the pH-independent formation constants for ferric and ferrous heme $b-[H10A24]_2$ are estimated to be 1.2×10^{13} and 2.9×10^{10} M^{-1}, respectively, and their ratio is quite similar to that observed for heme $b-[\Delta7\text{-His}]_2$, consistent with the observation that they have similar E_m values at high pH, a ΔE_m of 18 mV.

Last, this analysis reveals that the difference in the mechanisms for coupling of proton to heme oxidation and/or reduction observed in these two scaffolds reflects the differences in the absolute ferrous heme *b* affinity. Weak ferrous heme affinity and $2H^+/1e^-$ redox events due to a ligand loss mechanism are likely in designed bis-His heme proteins with either very negative midpoint reduction potentials, where $K_d^{Fe(III)}/K_d^{Fe(II)}$ is small, or minimal hydrophobic cores, where ΔG^{assoc} is small. In the case of heme $b-[\Delta7\text{-His}]_2$, the different sources in the stabilities of ferric and ferrous heme $b-[\Delta7\text{-His}]_2$ manifest the $2H^+/1e^-$ redox event. The 2.8×10^7 M^{-1} (10.1 kcal/mol) formation constant of ferrous heme $b-[\Delta7\text{-His}]_2$ is the sum of the 7.4 kcal/mol contribution from heme association and the 2.7 kcal/mol contributed by the axial ligands, while the formation constant in the ferric state, 13.5 kcal/mol, is primarily due to the axial ligands, 11.2 kcal/mol, with a minor contribution from heme association, 2.3 kcal/mol. The weaker axial ligation to ferrous heme results in dissociation of heme from the histidine ligands upon reduction and the observed Pourbaix diagram. A ligand loss mechanism is also evident in cytochrome *c*″, where reduction leads to dissociation of a single His ligand and ligand loss at Cu_B has been proposed by Wikström to be active in the proton pumping of cytochrome *c* oxidase, i.e., the histidine cycle mechanism (*76*−*78*). The difference in proton coupling between heme $b-[\Delta7\text{-His}]_2$ and cytochrome *c*″ may reflect the covalent linkage of the heme to the protein scaffold. One role of the thioether linkages in *c*-type cytochromes may be to provide additional ΔG^{assoc} over the corresponding *b*-type cytochromes since the heme cannot be fully dissociated from the protein scaffold. Therefore, these data provide support for Benson's effective concentration hypothesis about the long-standing question of why Nature developed *c*-type cytochromes (*79*, *80*).

In the case of heme $b-[H10A24]_2$, the Pourbaix diagram is due to the electrostatic response of the scaffold to bound heme oxidation and/or reduction as both ferric and ferrous heme bind tightly at pH >4.0. The tight ferrous heme binding observed is dominated by the heme association term (9.2 kcal/mol) with minor contributions from iron coordination (1.4 kcal/mol) and electrostatic effects (3.7 kcal/mol), while the tight ferric affinity is due to heme association (6.7 kcal/mol), histidine coordination (3.6 kcal/mol), and electrostatic stabilization (7.6 kcal/mol). The increased heme association terms, 9.2 and 6.7 kcal/mol, yield the tight ferric and ferrous heme affinities, picomolar K_d values, that require that the protein scaffold compensate for the charge introduced upon heme oxidation by glutamic acid or lysine deprotonation. This electrostatic response mechanism, shown in Scheme 2A, is the one typically invoked when proton-coupled electron transfer events are observed in metalloproteins. While this is the case for heme $b-[H10A24]_2$, the data for heme $b-[\Delta7\text{-His}]_2$ suggest that ligand loss is also a viable mechanism.

Furthermore, the data imply that there may be a threshold value of ΔG^{assoc} at which a protein scaffold will change its proton coupling mechanism.

CONCLUSION

In conclusion, the thermodynamic analysis presented herein allows the individual contributions of heme association, heme coordination, and heme−protein electrostatic effects to be elucidated in designed ferric and ferrous heme protein scaffolds. The data reveal the absolute stabilization and/or destabilization of heme in the ferric and ferrous oxidation states responsible for their midpoint reduction potential values. These data demonstrate that differences in ferric and ferrous heme association between the two scaffolds result in a change in their mechanisms of proton-coupled electron transfer. The tighter association of heme with $[H10A24]_2$ maintains the bis-His axial coordination in both oxidation states which leads to its electrostatic response mechanism of proton−electron coupling. Weaker protein−porphyrin association in $[\Delta 7\text{-His}]_2$ leads to dissociation of the His ligands upon reduction and proton-coupled electron transfer based on a ligand loss mechanism.

REFERENCES

1. Dutton, P. L., and Wilson, D. F. (1974) Redox potentiometry in mitochondrial and photosynthetic bioenergetics, *Biochim. Biophys. Acta 346*, 165−212.
2. Papa, S., Guerrieri, F., and Izzo, G. (1979) Redox Bohr-effects in the cytochrome system of mitochondria, *FEBS Lett. 105*, 213−216.
3. Nocera, D. G., and Cukier, R. I. (1998) Proton-Coupled Electron Transfer, *Annu. Rev. Phys. Chem. 49*, 337−369.
4. Brandt, U. (1997) Proton-translocation by membrane-bound NADH:ubiquinone-oxidoreductase (complex I) through redox-gated ligand conduction, *Biochim. Biophys. Acta 1318*, 79−91.
5. Pankhurst, K. L., Mowat, C. G., Rothery, E. L., Hudson, J. M., Jones, A. K., Miles, C. S., Walkinshaw, M. D., Armstrong, F. A., Reid, G. A., and Chapman, S. K. (2006) A proton delivery pathway in the soluble fumarate reductase from *Shewanella frigidimarina*, *J. Biol. Chem. 281*, 20589−20597.
6. Dutton, P. L., Moser, C. C., Sled, V. D., Daldal, F., and Ohnishi, T. (1998) A reductant-induced oxidation mechanism for Complex I, *Biochim. Biophys. Acta 1364*, 245−257.
7. Kim, J., Mao, J., and Gunner, M. R. (2005) Are acid and basic groups in buried proteins predicted to be ionized? *J. Mol. Biol. 348*, 1283−1298.
8. Mitchell, P. (1961) Coupling of phosphorylation to electron and hydrogen transfer by a chemi-osmotic type of mechanism, *Nature 191*, 144−148.
9. Okamura, M. Y., and Feher, G. (1992) Proton transfer in reaction centers from photosynthetic bacteria, *Annu. Rev. Biochem. 61*, 861−896.
10. Beinert, H., Holm, R. H., and Münck, E. (1997) Iron-sulfur clusters: Nature's modular multipurpose structures, *Science 277*, 653−659.
11. Chapman, S. K., Daff, S., and Munro, A. W. (1997) Heme: The most versatile redox center in biology, *Struct. Bonding 88*, 39−70.
12. Magliozzo, R. S., McIntosh, B. A., and Sweeney, W. V. (1982) Origin of the pH dependence of the midpoint reduction potential in *Clostridium pasteurianum* ferredoxin: Oxidation state-dependent hydrogen ion association, *J. Biol. Chem. 257*, 3506−3509.
13. Moore, G. R., and Pettigrew, G. W. (1990) *Cytochromes c. Evolutionary, Structural, and Physicochemical Aspects*, Springer-Verlag, Berlin.
14. Camba, R., Jung, Y. S., Hunsicker-Wang, L. M., Burgess, B. K., Stout, C. D., Hirst, J., and Armstrong, F. A. (2003) Mechanisms of redox-coupled proton transfer in proteins: Role of the proximal proline in reactions of the [3Fe-4S] cluster in *Azotobacter vinelandii* Ferredoxin I, *Biochemistry 42*, 10589−10599.
15. Chen, K., Hirst, J., Camba, R., Bonagura, C. A., Stout, C. D., Burgess, B. K., and Armstrong, F. A. (2000) Atomically defined mechanism for proton transfer to a buried redox centre in a protein, *Nature 405*, 814−817.
16. Zu, Y., Fee, J. A., and Hirst, J. (2001) Complete thermodynamic characterization of reduction and protonation of the bc_1-type Rieske [2Fe-2S] center of *Thermus thermophilus*, *J. Am. Chem. Soc. 123*, 9906−9907.
17. Coletta, M., Costa, H., De Sanctis, G., Neri, F., Smulevich, G., Turner, D. L., and Santos, H. (1997) pH dependence of structural and functional properties of oxidized cytochrome *c″* from *Methylophilus methylotrophus*, *J. Biol. Chem. 272*, 24800−24804.
18. Louro, R. O., Catarino, T., LeGall, J., Turner, D. L., and Xavier, A. V. (2001) Cooperativity between electrons and protons in a monomeric cytochrome c_3: The importance of mechano-chemical coupling for energy transduction, *ChemBioChem 2*, 831−837.
19. Louro, R. O., Catarino, T., Turner, D. L., Picarra-Pereira, M. A., Pacheco, I., LeGall, J., and Xavier, A. V. (1998) Functional and mechanistic studies of cytochrome c_3 from *Desulfovibrio gigas:* Thermodynamics of a "proton thruster", *Biochemistry 37*, 15808−15815.
20. Shifman, J. M., Moser, C. C., Kalsbeck, W. A., Bocian, D. F., and Dutton, P. L. (1998) Functionalized *de novo* designed proteins: Mechanism of proton coupling to oxidation/reduction in heme protein maquettes, *Biochemistry 37*, 16815−16827.
21. Gibney, B. R., Huang, S. S., Skalicky, J. J., Fuentes, E. J., Wand, A. J., and Dutton, P. L. (2001) Hydrophobic modulation of heme properties in heme protein maquettes, *Biochemistry 40*, 10550−10561.
22. Lombardi, A., Nastri, F., Marasco, D., Maglio, O., De Sanctis, G., Sinibaldi, F., Santucci, R., Coletta, M., and Pavone, V. (2003) Design of a new mimochrome with a unique topology, *Chem.−Eur. J. 9*, 5643−5654.
23. Kennedy, M. L., and Gibney, B. R. (2002) Proton coupling to $[4Fe\text{-}4S]^{2+/+}$ and $[4Fe\text{-}4Se]^{2+/+}$ oxidation and reduction in a designed protein, *J. Am. Chem. Soc. 124*, 6826−6827.
24. Calhoun, M. W., Thomas, J. W., and Gennis, R. B. (1994) The cytochrome oxidase superfamily of redox-driven proton pumps, *Trends Biochem. Sci. 19*, 325−330.
25. Wikström, M. (2000) Proton translocation by cytochrome *c* oxidase: A rejoinder to recent criticism, *Biochemistry 39*, 3515−3519.
26. Michel, H. (1999) Cytochrome c oxidase: Catalytic cycle and mechanisms of proton pumping-A discussion, *Biochemistry 38*, 15129−15140.
27. Robertson, D. E., Farid, R. S., Moser, C. C., Urbauer, J. L., Mulholland, S. E., Pidikiti, R., Lear, J. D., Wand, A. J., DeGrado, W. F., and Dutton, P. L. (1994) Design and synthesis of multi-haem proteins, *Nature 368*, 425−432.
28. Reedy, C. J., and Gibney, B. R. (2004) Heme protein assemblies, *Chem. Rev. 104*, 617−649.
29. Reedy, C. J., Kennedy, M. L., and Gibney, B. R. (2003) Thermodynamic characterization of ferric and ferrous haem binding to a designed four-α-helix protein, *Chem. Commun.*, 570−571.
30. Lombardi, A., Nastri, F., and Pavone, V. (2001) Peptide-based heme protein models, *Chem. Rev. 101*, 3165−3190.
31. Yu, L., Mei, Q. C., and Yu, C. A. (1984) Characterization of purified cytochrome bc_1 complex from *Rhodopseudomonas sphaeroides* R-26, *J. Biol. Chem. 259*, 5752−5760.
32. Zhuang, J. (2005) Investigation of the effects of non-natural amino acids and hemes in *de novo* heme protein design, Ph.D. Thesis, Columbia University, New York.
33. Zhuang, J., Amoroso, J. H., Kinloch, R., Dawson, J. H., Baldwin, M. J., and Gibney, B. R. (2006) Evaluation of electron-withdrawing group effects on heme binding in a designed protein: Implications for heme *a* in cytochrome *c* oxidase, *Inorg. Chem. 45*, 4685−4694.
34. Zhuang, J., Reddi, A. R., Wang, Z., Khodaverdian, B., Hegg, E. L., and Gibney, B. R. (2006) Evaluating the roles of the heme *a* side chains in cytochrome c oxidase using designed heme proteins, *Biochemistry 45*, 12530−12538.
35. Kates, S. A., and Albericio, F. (2000) *Solid-phase synthesis: A practical guide*, pp 826, Marcel Dekker, New York.
36. Dutton, P. L. (1978) Redox potentiometry: Determination of midpoint potentials of oxidation-reduction components of biological electron-transfer systems, *Methods Enzymol. 54*, 411−435.
37. de Levie, R. (2003) The Henderson-Hasselbalch equation: Its history and limitations, *J. Chem. Educ. 80*, 146.

38. Berry, E. A., and Trumpower, B. L. (1987) Simultaneous determination of hemes *a*, *b*, and *c* from pyridine hemochrome spectra, *Anal. Biochem. 161*, 1−15.
39. Nesset, M. J. M., Shokhirev, N. V., Enemark, P. D., Jacobson, S. E., and Walker, F. A. (1996) Models of the cytochromes. Redox properties and thermodynamic stabilities of complexes of "hindered'' iron(III) and iron(II) tetraphenylporphyrinates with substituted pyridines and imidazoles, *Inorg. Chem. 35*, 5188−5200.
40. Hargrove, M. S., and Olson, J. S. (1996) The stability of holomyoglobin is determined by heme affinity, *Biochemistry 35*, 11310−11318.
41. Wittung-Stafshede, P. (2002) Role of cofactors in protein folding, *Acc. Chem. Res. 35*, 201−208.
42. Wilson, C., Apiyo, D., and Wittung-Stafshede, P. (2004) Role of cofactors in metalloprotein folding, *Rev. Biophys. 37*, 285−314.
43. Mines, G. A., Pascher, T., Lee, S. C., Winkler, J. R., and Gray, H. B. (1996) Cytochrome c folding triggered by electron transfer, *Chem. Biol. 3*, 491−497.
44. Winkler, J. R., Wittung-Stafshede, P., Leckner, J., Malmström, B. G., and Gray, H. B. (1999) Effects of folding on metalloprotein active sites, *Proc. Natl. Acad. Sci. U.S.A. 94*, 4246−4249.
45. Uchiyama, S., Ohshima, A., Nakamura, S., Hasegawa, J., Terui, N., Takayma, S. J., Yamamoto, Y., Sambongi, Y., and Kobayashi, Y. (2004) Complete thermal-unfolding profiles of oxidized and reduced cytochromes c, *J. Am. Chem. Soc. 126*, 14684−14685.
46. Zhuang, J., Amoroso, J. H., Kinloch, R., Dawson, J. H., Baldwin, M. J., and Gibney, B. R. (2004) Design of a five-coordinate heme protein maquette: A spectroscopic model of deoxymyoglobin, *Inorg. Chem. 43*, 8218−8220.
47. Privett, H. K., Reedy, C. J., Kennedy, M. L., and Gibney, B. R. (2002) Non-natural amino acid ligands in heme protein design, *J. Am. Chem. Soc. 124*, 6828−6829.
48. Hargrove, M. S., Barrick, D., and Olson, J. S. (1996) The association rate constant for heme binding to globin is independent of protein structure, *Biochemistry 35*, 11293−11299.
49. Silchenko, S., Sippel, M. L., Kuchment, O., Benson, D. R., Mauk, A. G., Altuve, A., and Rivera, M. (2000) Hemin is kinetically trapped in cytochrome b_5 from rat outer mitochondrial membrane, *Biochem. Biophys. Res. Commun. 273*, 467−472.
50. Robinson, C. R., Liu, Y., Thomson, J. A., Sturtevant, J. M., and Sligar, S. G. (1997) Energetics of heme binding to native and denatured states of cytochrome b_{562}, *Biochemistry 36*, 16141−16146.
51. Battistuzzi, G., Borsari, M., Cowan, J. A., Ranieri, A., and Sola, M. (2002) Control of cytochrome c redox potential: Axial ligation and protein environmental effects, *J. Am. Chem. Soc. 124*, 5315−5324.
52. Bryson, J. W., Betz, S. F., Lu, H. S., Suich, D. J., Zhou, H. X., O'Neil, K. T., and DeGrado, W. F. (1995) Protein design: A hierarchic approach, *Science 270*, 935−941.
53. Rojas, N. R. L., Kamtekar, S., Simons, C. T., McLean, J. E., Vogel, K. M., Spiro, T. G., Farid, R. S., and Hecht, M. H. (1997) De novo heme proteins from designed combinatorial libraries, *Protein Sci. 6*, 2512−2524.
54. Rosenblatt, M. M., Wang, J., and Suslick, K. S. (2003) De novo designed cyclic-peptide heme complexes, *Proc. Natl. Acad. Sci. U.S.A. 100*, 13140−13145.
55. Benson, D. R., Hart, B. R., Zhu, X., and Doughty, M. B. (1995) Design, synthesis and circular dichroism investigation of a peptide-sandwiched mesoheme, *J. Am. Chem. Soc. 117*, 8502−8510.
56. Huang, S. S., Koder, R. L., Lewis, M. L., Wand, A. J., and Dutton, P. L. (2004) The HP-1 maquette: From an apo-protein structure to a structured hemoprotein designed to promote redox-coupled proton exchange, *Proc. Natl. Acad. Sci. U.S.A. 101*, 5536−5541.
57. Antonini, E., and Brunori, M. (1971) *Hemoglobin and myoglobin in their reactions with ligands*, North-Holland, Amsterdam.
58. Kassner, R. J. (1972) Effects of nonpolar environments on the redox potentials of heme complexes, *Proc. Natl. Acad. Sci. U.S.A. 69*, 2263−2267.
59. Stellwagen, E. (1978) Heme exposure as determinate of oxidation-reduction potential of heme proteins, *Nature 275*, 73−74.
60. Tezcan, F. A., Winkler, J. R., and Gray, H. B. (1998) Effects of ligation and folding on reduction potentials of heme proteins, *J. Am. Chem. Soc. 120*, 13383−13388.
61. Stroebel, D., Chouquet, Y., Popot, J.-L., and Picot, D. (2003) An atypical haem in the cytochrome b_6f complex, *Nature 426*, 413−418.
62. Alric, J., Pierre, Y., Picot, D., Lavergne, J., and Rappaport, F. (2005) Spectral and redox characterization of the heme c_i in the cytochrome b_6f complex, *Proc. Natl. Acad. Sci. U.S.A. 102*, 15860−15865.
63. Skalicky, J. J., Gibney, B. R., Rabanal, F., Bieber-Urbauer, R. J., Dutton, P. L., and Wand, A. J. (1999) Solution structure of a designed four-α-helix bundle maquette scaffold, *J. Am. Chem. Soc. 121*, 4941−4951.
64. Huang, S. S., Gibney, B. R., Stayrook, S. E., Dutton, P. L., and Lewis, M. (2003) X-ray structure of a maquette scaffold, *J. Mol. Biol. 326*, 1219−1225.
65. Scott, R. A., and Mauk, A. G. (1996) *Cytochrome c: A multidisciplinary approach*, University Science Books, Sausalito, CA.
66. Choma, C. T., Lear, J. T., Nelson, M. J., Dutton, P. L., Robertson, D. E., and DeGrado, W. F. (1994) Design of a heme binding four helix bundle, *J. Am. Chem. Soc. 116*, 856−865.
67. Shifman, J. M., Gibney, B. R., Sharp, R. E., and Dutton, P. L. (2000) Redox potential control in de novo designed four-α-helix bundle proteins, *Biochemistry 39*, 14813−14821.
68. Gunner, M. R., Alexov, E., Torres, E., and Lipovaca, S. (1997) The importance of the protein in controlling the electrochemistry of heme metalloproteins: Methods of calculation and analysis, *J. Biol. Inorg. Chem. 2*, 126−134.
69. Coryell, C. D., and Pauling, L. (1940) A structural interpretation of the acidity of groups associated with the hemes of hemoglobin and hemoglobin derivatives, *J. Biol. Chem. 132*, 769−779.
70. Wyman, J., Jr., and Allen, D. W. (1951) The problem of the heme interactions in hemoglobin and the basis of the Bohr effect, *J. Polym. Sci. 7*, 499−518.
71. Perutz, M. F., Muirhead, H., Mazzarella, L., Crowther, R. A., Greer, J., and Kilmartin, J. V. (1969) Identification of residues responsible for the alkaline Bohr effect in haemoglobin, *Nature 222*, 1240−1243.
72. Nastri, F., Lombardi, A., Morelli, G., Maglio, O., D'Auria, G., Pedone, C., and Pavone, V. (1997) Hemoprotein models based on a covalent helix-heme-helix-sandwich: 1. Design, synthesis, and characterization, *Chem.—Eur. J. 3*, 340−349.
73. Moffet, D. A., Foley, J., and Hecht, M. H. (2003) Midpoint reduction potentials and heme binding stoichiometries of de novo proteins from designed combinatorial libraries, *Biophys. Chem. 105*, 231−239.
74. Wilson, J. R., Caruana, D. J., and Gilardi, G. (2003) Engineering redox functions in a nucleic acid binding protein, *Chem. Commun.*, 356−357.
75. Ghirlanda, G., Osyczka, A., Liu, W., Antolovich, M., Smith, K. M., Dutton, P. L., Wand, A. J., and DeGrado, W. F. (2004) De novo design of a D_2-symmetrical protein that reproduces the diheme four-helix bundle of cytochrome bc_1, *J. Am. Chem. Soc. 126*, 8141−8147.
76. Wikström, M., Bogachev, A., Finel, M., Morgan, J. E., Puustinen, A., Raitio, M., Verkhovskaya, M., and Verkhovsky, M. I. (1994) Mechanism of proton translocation by the respiratory oxidases. The histidine cycle, *Biochim. Biophys. Acta 1187*, 106−111.
77. Wikström, M. (1977) Proton pump coupled to cytochrome c oxidase in mitochondria, *Nature 266*, 271−273.
78. Iwata, S., Ostermeier, C., Ludwig, B., and Michel, H. (1995) Structure at 2.8 Å resolution of cytochrome c oxidase from *Paracoccus denitrificans*, *Nature 376*, 660−669.
79. Cowley, A. B., Lukat-Rodgers, G. S., Rodgers, K. R., and Benson, D. R. (2004) A possible role for the covalent heme-protein linkage in cytochrome *c* revealed via comparison of *N*-acetylmicroperoxidase-8 and a synthetic, monohistidine-coordinated heme peptide, *Biochemistry 43*, 1656−1666.
80. Allen, J. W. A., Barker, P. D., Daltrop, O., Stevens, J. M., Tomlinosn, E. J., Sinha, N., Sambongi, Y., and Ferguson, S. J. (2005) Why isn't 'standard' heme good enough for c-type and d_1-type cytochromes? *Dalton Trans. 21*, 3410−3418.

BI061607G